Revision #1

Mineralogy, paragenesis and mineral chemistry of REE minerals in the Olserum–Djupedal REE-phosphate mineralization, SE Sweden

Stefan S. Andersson[1], Thomas Wagner[2], Erik Jonsson[3,4], and Radoslaw M. Michallik[1]

[1]Department of Geosciences and Geography, University of Helsinki, P.O. Box 64 (Gustaf Hällströmin katu 2a), FI-00014 Helsinki, Finland

[2]Institute of Applied Mineralogy and Economic Geology, RWTH Aachen University, Wüllnerstr. 2, D-52062 Aachen, Germany

[3]Department of Mineral Resources, Geological Survey of Sweden, Box 670, SE-75128 Uppsala, Sweden

[4]Department of Earth Sciences, Uppsala University, Villavägen 16, SE-75266 Uppsala, Sweden

Abstract

The rapidly growing use of rare earth elements and yttrium (REE) in modern-day technologies, not least within the fields of green and carbon-free energy applications, requires exploitation of new REE deposits and deposit types. In this perspective, it is vital to develop fundamental understanding of the behavior of REE in natural hydrothermal systems and the formation of hydrothermal REE deposits. In this study, we establish a mineralogical, textural, and mineral-chemical framework for a new type of deposit, the hydrothermal Olserum-Djupedal REE-phosphate mineralization in SE Sweden. An early, high-temperature REE stage is characterized by abundant monazite-(Ce) and xenotime-(Y) coexisting with fluorapatite and subordinate amounts of (Y,REE,U,Fe)-(Nb,Ta) oxides. During a subsequent stage, allanite-(Ce) and ferriallanite-(Ce) formed locally, partly resulting from the breakdown of primary monazite-(Ce). Alteration of allanite-(Ce) or ferriallanite-(Ce) to bastnäsite-(Ce) and minor synchysite-(Ce) at lower temperatures represents the latest stage of REE mineral formation. The paragenetic sequence and mineral chemistry of the allanites record an increase in Ca content in the fluid. We suggest that this local increase in Ca, in conjunction with changes in oxidation state, were the key factors controlling the stability of monazite-(Ce) in the assemblages of the Olserum-Djupedal deposit. We interpret the alteration and replacement of primary monazite-(Ce), xenotime-(Y), fluorapatite, and minor (Y,REE,U,Fe)-(Nb,Ta) oxide phase(s), to be the consequence of coupled dissolution-reprecipitation processes. These processes mobilized REE, Th, U, and Nb-Ta, which caused the formation of secondary monazite-(Ce), xenotime-(Y), fluorapatite, and minor amounts of allanite-(Ce) and ferriallanite-(Ce). In addition, these alteration processes produced uraninite, thorite, columbite-(Fe), and uncharacterized (Th,U,Y,Ca)-silicates. Textural relations show that the dissolution-reprecipitation processes affecting fluorapatite preceded those affecting monazite-(Ce), xenotime-(Y), and the (Y,REE,U,Fe)-(Nb,Ta) oxide phase(s). The mineralogy of the primary ore mineralization and the subsequently formed alteration assemblages demonstrate the combined mobility of REE and HFSE in a natural F-bearing high-temperature hydrothermal system. The observed coprecipitation of monazite-(Ce), xenotime-(Y), and fluorapatite during the primary REE mineralization stage highlights the need for further research on the potentially important role of phosphate in hydrothermal REE transporting systems.

Keywords: Rare earth elements, hydrothermal, monazite, xenotime, allanite, apatite, Olserum, Sweden

Introduction

In recent years, the global demand for the rare earth elements and yttrium (REE) for the rapidly growing green and carbon-free energy and information technologies has prompted extensive re-evaluation of REE deposits, and new research on the geochemical transport behavior and enrichment processes of these elements. Primary enrichment of REE to form mineral deposits can result from magmatic processes, such as in peralkaline silica-undersaturated rocks, peralkaline granites, pegmatites, and in carbonatites (e.g., Chakhmouradian and Zaitzsev 2012, and references therein). Importantly, carbonatite-associated REE mineralizations are in most cases further enriched in the REE through late-stage hydrothermal fluid mobilization. Prominent examples include the mineralization in Lofdal, Namibia (Wall et al. 2008) or the mineralization at the Fen complex, Norway (e.g., Andersen 1984). In addition, ample evidence supporting a combined magmatic-hydrothermal origin is also present for other deposit types, such as the Strange Lake REE-Zr-Nb deposit, Canada (e.g., Salvi and Williams-Jones 1990; Gysi et al. 2016), and several REE enriched magmatic iron-oxide apatite deposits (e.g., Harlov et al. 2002, 2016; Jonsson et al. 2016). There are also a number of recognized deposits that primarily formed by hydrothermal processes. These include for instance the Bayan Obo REE-Nb-Fe deposit, China (e.g., Chao et al. 1992; Smith and Henderson 2000; Smith et al. 2015) and the REE deposit in the Gallinas Mountains, USA (Williams-Jones et al. 2000). The importance of hydrothermal REE transport and deposition is also highlighted by new experimental evidence for the high solubility of REE and high field strength elements (HFSE), such as Zr, Nb, and Ta, in certain hydrothermal fluids (e.g., Migdisov et al. 2009, 2011; Loges et al. 2013; Timofeev et al. 2015, 2017).

The principal host of REE in many phosphate-rich hydrothermal REE deposits is the light rare earth element (LREE) dominated monazite, for instance in Kangankunde, Malawi (Wall and Mariano 1996), Kutessay II, Kyrgyzstan (Djenchuraeva et al. 2008, and references therein) and in the Fen complex, Norway (Andersen 1986). In contrast, a fewer number of recognized deposits also contain or are dominated by the heavy rare earth element (HREE) rich xenotime, such as the Lofdal deposit in Namibia (Wall et al. 2008), the Songwe Hill carbonatite in Malawi (e.g., Broom-Fendley et al. 2017), the xenotime-florencite deposit in Browns Ranges, Australia (Cook et al. 2013) or the monazite-xenotime mineralization in Music Valley, USA (McKinney et al. 2015). Thus, studies that improve our fundamental understanding of the behavior of REE-phosphates, especially those that are HREE-enriched, in natural hydrothermal systems are essential. Of particular importance are studies that elucidate factors controlling REE transport and precipitation such as fluid chemistry, ligand activity, temperature, and pressure. Key questions include the role of magmatic-hydrothermal fluids in REE mineralizing systems, the role of F complexing for hydrothermal REE transport, and the role of phosphate as a transporting agent or precipitant for REE-phosphate mineralization.

This study addresses the formation of REE-phosphate deposits, focusing on the metasediment- and granite-hosted Olserum-Djupedal REE mineralization in southeastern Sweden, which includes one of very few REE deposits in Europe with an internationally recognized resource classification (NI 43-101; Reed 2013). Notably, the Proterozoic bedrock of the Fennoscandian shield is one of the most important areas today in Europe for the exploration and mining of both base and rare or critical metals, including the REE (e.g., Goodenough et al. 2016). As a first step to characterize and understand the mineralization of the Olserum area, we have established a mineralogical, textural, and mineral-chemical framework of the REE bearing minerals by combining field geology, mineralogical, and petrographical/textural analysis, and major and trace element analysis of REE phases by electron-microprobe and laser-ablation inductively coupled plasma mass spectrometry (LA-ICP-MS). This makes it possible to at least partly infer the conditions and chemistry of the fluids that caused the formation and subsequent post-depositional modification of the mineral assemblages and textures of this new type of REE mineralization.

Geological background

The Olserum-Djupedal REE mineralization (Fig. 1) is located at the boundary between the Paleoproterozoic Västervik formation and the Transscandinavian Igneous Belt (TIB) south of the Svecofennian domain proper, in the Fennoscandian shield (Gavelin 1984; Gaál and Gorbatschev 1987; Högdahl et al. 2004). The Svecofennian domain evolved from an Archean nucleus in the northwest, via several accretional stages during the time interval 1.92-1.77 Ga, and generally shows younging towards the present-day southwest (e.g., Nironen 1997; Korja et al. 2006; Lahtinen et al. 2009). The Svecofennian domain is bounded to the west and south by the large, N-S trending TIB batholithic structure that developed during a long-lived active continental margin from c. 1.85 to c. 1.65 Ga (Högdahl et al. 2004).

The approximately 1.8 Ga old Loftahammar-Linköping deformation zone (LLDZ; Beunk and Page 2001) separates the Svecofennian domain from the Västervik formation. The Västervik formation consists predominantly of metasedimentary rocks, mainly quartzites and metarenites, with subordinate metavolcanic rocks (Gavelin 1984), which were deposited between c. 1.88 and 1.85 Ga (Sultan et al. 2005) in an extensional regime (Beunk and Page 2001). The metavolcanosedimentary succession was subsequently intruded by various granitoids, traditionally referred to as consisting of an older, c. 1.85 Ga old, deformed Loftahammar type and a geologically younger, c. 1.81-1.77 Ga suite of so-called TIB-1 granitoids (Gavelin 1984; Kresten 1986; Åhäll and Larsson 2000; Andersson and Wikström 2004; Högdahl et al. 2004). Nolte et al. (2011) recently proposed a new classification of the Västervik granitoids, followed by new zircon U-Pb age determinations (Kleinhanns et al. 2015). These authors suggest a tectonic evolution that commenced with a back-arc extensional regime around 1.88-1.85 Ga with related ferroan (or A-type) magmatism, followed by a compressional regime around 1.85-1.81 Ga, featuring the intrusion of magnesian-type (or Cordilleran-type) granitoids. Subsequently, crustal relaxation occurred around 1.8 Ga and was accompanied by shallow ferroan (or A-type) anatectic granites, likely coeval with low pressure/high temperature metamorphism and migmatization (Kresten 1971; Gavelin 1984; Kleinhanns et al. 2012).

In contrast to the extensively mineralized Paleoproterozoic Bergslagen province further north and northwest (e.g., Stephens et al. 2009), the Västervik area only hosts a limited number of Fe ± U ± REE mineralizations (Uytenbogaardt 1960; Welin and Uytenbogaardt 1963; Welin 1966a, 1966b; Hoeve 1974), as well as some Fe ± Cu ± Co ± Mo mineralizations (Uytenbogaardt 1960; Sundblad 2003, and references therein; Billström et al. 2004). Published genetic interpretations of the Fe ± U ± REE mineralizations include: (1) a placer origin with some remobilization during the intrusion of the youngest granites (Welin 1966a, 1966b), (2) a magmatic origin related to the younger granites (Uytenbogaardt 1960), or (3) a hydrothermal origin concomitant with regional Na ± Ca metasomatism during the intrusion of the younger granites (Hoeve 1974, 1978; Fig. 1). Previous studies of the Olserum-Djupedal mineralization mainly focused on identifying the principal REE minerals (Reed 2013; Fullerton 2014) and obtaining major element mineral chemistry data for xenotime, monazite, and fluorapatite as well as other minerals (Fullerton 2014). Yet, these studies only covered a small part of the known mineralization. The Olserum deposit was at the same time targeted for exploration, yielding an indicated resource estimate of 4.5 Mt at 0.6% total rare earth oxides (TREO) with 33.9% heavy rare earth oxides (HREO) (Reed 2013). This, however, only represents a part of the known mineralized area, and the resource is open at depth. The mineralization is hosted partly by quartz + biotite + plagioclase ± cordierite metasedimentary rocks (Olserum area) of the Västervik formation and by 1.8 Ga TIB granites (Olserum and Djupedal areas), most likely granites that belong to the anatectic A-type granites (AG group; Nolte et al. 2011).

Analytical methods

Electron-probe microanalysis (EPMA)

Mineral chemical analyses were conducted on monazite, xenotime, allanite, and REE-fluorocarbonates. This was done by wavelength-dispersive electron probe microanalysis (EPMA) using a JEOL JXA-8600 Superprobe at the University of Helsinki, upgraded with SAMx hardware and the XMAs/IDFix/Diss5 analytical and imaging software package. The accelerating voltage was 20 kV and the beam current 25 nA. A defocused beam of about 7 μm diameter was used for monazite and xenotime, and a focused beam for allanite and REE-fluorocarbonates. As described by Pyle et al. (2002), X-ray lines for REE analysis in monazite and xenotime were chosen to minimize the interferences between the different REE. A full list of the selected lines and other settings used for EPMA analysis are presented in the Electronic Supplementary Material (Tables EA1 and EA2). Detection limits for REE, Y, Th and U, varied between about 500 and 2000 ppm, and were lower than 800 ppm for the other elements.

Laser ablation inductively coupled plasma mass spectrometry (LA-ICP-MS)

LA-ICP-MS analysis of monazite, xenotime, allanite, clinozoisite, and bastnäsite were performed with a Coherent GeoLas MV 193 nm laser-ablation system coupled to an Agilent 7900s ICP mass spectrometer at the University of Helsinki. Flow rates were set to 15 L/min for Ar plasma gas, 1.0 L/min for He carrier gas, and 0.85 L/min for Ar auxiliary gas for all measurements. A laser fluence of 5 J/cm^2 and a repetition rate of 5 Hz with 300 pulses were used for monazite and xenotime. The following isotopes were measured: ^{27}Al, ^{29}Si, ^{31}P, ^{34}S, ^{44}Ca, ^{45}Sc, ^{51}V, ^{57}Fe, ^{89}Y, ^{90}Zr, ^{93}Nb, ^{139}La, ^{140}Ce, ^{141}Pr, ^{146}Nd, ^{147}Sm, ^{151}Eu, ^{157}Gd, ^{159}Tb, ^{163}Dy, ^{165}Ho, ^{166}Er, ^{169}Tm, ^{172}Yb, ^{175}Lu, ^{178}Hf, ^{181}Ta, ^{182}W, ^{208}Pb, ^{232}Th, and ^{238}U. ^{75}As was omitted because of the strong interference by doubly-charged ^{150}Nd and ^{150}Sm. Potential interferences on ^{178}Hf, ^{181}Ta and, ^{182}W are discussed in the Electronic Supplementary Material. A laser fluence of 4 J/cm^2 and a repetition rate of 8 Hz with 400 pulses were used for allanite, clinozoisite, and bastnäsite. The program included the following isotopes: ^{23}Na, ^{24}Mg, ^{27}Al, ^{29}Si, ^{31}P, ^{42}Ca, ^{45}Sc, ^{49}Ti, ^{51}V, ^{55}Mn, ^{57}Fe, ^{66}Zn, ^{88}Sr, ^{89}Y, ^{118}Sn, ^{137}Ba, ^{39}La, ^{140}Ce, ^{141}Pr, ^{146}Nd, ^{147}Sm, ^{151}Eu, ^{157}Gd, ^{159}Tb, ^{163}Dy, ^{165}Ho, ^{166}Er, ^{169}Tm, ^{172}Yb, ^{175}Lu, ^{208}Pb, ^{232}Th, and ^{238}U. Spot sizes for all measurements were typically 44 μm or 66 μm, but sometimes 32 μm and 24 μm for smaller or zoned grains.

Sample analyses for monazite, xenotime, and bastnäsite were bracketed with replicate analysis of reference material NIST SRM 610, and standard data were used to correct for instrumental drift. In addition, USGS reference glass GSE-1G was also repeatedly measured as a reference material for allanite, and was preferred as an external standard after careful data evaluation. Individually measured Ce, Y, and Al concentrations, determined by EPMA, were used as internal standard elements for quantification of element concentrations from LA-ICP-MS signals in monazite, xenotime, and allanite, respectively. The only exception was sample KJA01 (allanite from the biotite-magnetite schlieren), where average Al concentrations were used for quantification of the allanite data. The data treatment of LA-ICP-MS signals was done with the SILLS software package (Guillong et al. 2008). Each LA-ICP-MS signal was carefully checked for the presence of inclusions or heterogeneities, and integration windows were defined for homogeneous segments of the signals. The accuracy of the LA-ICP-MS data was verified and monitored daily by measuring the reference material NIST SRM 612 as an unknown sample. The long-term accuracy for the elemental concentration in SRM NIST 612 is well within the reported range of values and their associated uncertainties (Spandler et al. 2011). The complete analytical data set for both EPMA and LA-ICP-MS analyses is available as Electronic Supplementary Material.

Results

Paragenetic and textural evolution

The mineralization at Olserum-Djupedal is dominated by monazite-(Ce), xenotime-(Y), and fluorapatite hosted by veins that contain biotite + quartz + magnetite as the main gangue minerals, either occurring within quartz + biotite + plagioclase ± cordierite metasedimentary rocks (Figs. 2A and 2B), or within a K-feldspar- and biotite-rich granite (Fig. 2C). A broader ore zone or vein with biotite + amphibole (gedrite to ferrigedrite) + quartz + magnetite generally hosts larger crystals of monazite-(Ce), xenotime-(Y), and fluorapatite. Xenotime-(Y) crystals up to c. 8 cm in length are readily identified in Djupedal. Locally in Djupedal, paragenetically later allanite-(Ce) occurs (Fig. 2D).

The identified paragenetic sequence consists of four stages (A-D; Figs. 3 and 4). Stage A is the oldest stage and represents primary phosphate formation. Stage B is the first modification stage. It comprises the formation of secondary monazite-(Ce) and xenotime-(Y), local formation of allanite-group minerals, and REE minerals in granite-hosted schlieren. The alteration stage C comprises the alteration of previously formed minerals and the youngest stage D, represents the formation of REE-fluorocarbonates.

Stage A. The oldest recognized REE minerals are coarse-grained, tectonized, primary, subhedral to euhedral monazite-(Ce) and xenotime-(Y), and coeval fluorapatite. Both monazite-(Ce) and xenotime-(Y) occasionally display distinct zoning features, which vary from slightly concentric to sector-like (Figs. 5A and 5B). Not fully characterized (Y,REE,U,Fe)-(Nb,Ta) oxide phase(s) also formed during this stage. The fractures within primary monazite-(Ce), xenotime-(Y), and fluorapatite are filled with gangue minerals, mainly biotite, gedrite-ferrogedrite, quartz, magnetite, ilmenite, albite, muscovite, and cordierite. In addition, apparently later monazite-(Ce) and xenotime-(Y) frequently occur intergrown with magnetite and other gangue minerals (Fig. 5C). Similarly, granite-hosted veins consist of intergrown monazite-(Ce), xenotime-(Y), and magnetite with coexisting fluorapatite. These veins are often surrounded by a weak alteration envelope in the granite with albitized K-feldspar together with quartz, biotite, and muscovite.

Stage B. Stage B consists of the formation of secondary monazite-(Ce), xenotime-(Y) and, locally, massive allanite-(Ce). Secondary monazite-(Ce) and xenotime-(Y) are mostly manifested as inclusions within primary fluorapatite (Fig. 5D). These inclusions and other textural types of monazite-(Ce) and xenotime-(Y) that formed in relation to primary fluorapatite are hereafter referred to as fluorapatite-associated monazite-(Ce) or xenotime-(Y). The inclusions in fluorapatite are typically subhedral, and are often randomly oriented but are sometimes aligned parallel to the fluorapatite c-axis. By contrast, the rims and recrystallized grains of fluorapatite often lack both monazite-(Ce) and xenotime-(Y) inclusions. Similarly, such inclusions are frequently absent in zones parallel to adjacent fractures in fluorapatite. Within these zones, or in between recrystallized grains, slightly coarser grains of xenotime-(Y), and to a lesser extent monazite-(Ce), is present (Fig. 5D). In contrast, monazite-(Ce) occurs more frequently with minor xenotime-(Y) in the fractures of fluorapatite, or in the surrounding mineral matrix between the primary fluorapatite crystals (Fig. 5E). Within the matrix or in the fractures, both monazite-(Ce) and xenotime-(Y) are intergrown with magnetite (Fig. 5D and 5E), together with biotite, quartz, albite, andalusite, sulfides (pyrite and chalcopyrite), and muscovite.

Other secondary types of monazite-(Ce) and xenotime-(Y) occur as inclusions or along crystallographically aligned planes in primary monazite-(Ce), monazite-(Ce) replacing primary xenotime-(Y) (Fig. 5F), and monazite-(Ce) within fractures of primary xenotime-(Y). These later types of monazite-(Ce) and xenotime-(Y) are hereafter referred to as late-type monazite-(Ce) or xenotime-(Y). Furthermore, the fracture-fillings also comprise massive allanite-

(Ce) (Fig. 6A), quartz, biotite, amphibole (anthophyllite), magnetite, cordierite, and sometimes tourmaline and muscovite. Massive allanite-(Ce) also replaces an earlier magnetite.

The granite contains abundant biotite-magnetite schlieren (BMS) with somewhat variable primary mineral assemblages, which generally consist of coexisting xenotime-(Y) and monazite-(Ce) or solely allanite-(Ce). Other minor minerals in these schlieren are quartz, ilmenite, rutile, niobian rutile, fluorapatite, zircon, and sulfides. Since BMS-hosted monazite-(Ce), and, in part, xenotime-(Y) exhibit similar alteration features as other monazite-(Ce) or xenotime-(Y) formed during stage A or B, these schlieren are included in stage B. Another, yet similar, type of schlieren have more quartz-rich compositions, and are primarily composed of magnetite intergrown with monazite-(Ce) hosting small xenotime-(Y) inclusions.

Stage C. Slightly later or overlapping with stage B, extensive alteration of large primary monazite-(Ce) (Figs. 6B and 6C) occurred in Djupedal. Monazite-(Ce) is almost pervasively replaced by a second generation of fluorapatite, accompanied by the direct replacement of adjacent biotite by allanite-(Ce) and ferriallanite-(Ce). The formation of unzoned xenotime-(Y) is probably also related directly to this alteration (Fig. 6C); hereafter included with the late-type xenotime-(Y). It has also affected the late-type monazite-(Ce) (Figs. 5F and 6D), but exhibits a slightly different texture. Here, allanite-(Ce) occurs along the rims of monazite-(Ce) crystals together with minor fluorapatite and clinozoisite. Associated with these assemblages, ferberite, scheelite, quartz-muscovite symplectites, and staurolite occur as minor constituents. Staurolite is observed elsewhere as a breakdown product of cordierite, together with andalusite-quartz symplectites, gedrite or anthophyllite, and biotite. As previously mentioned, BMS-hosted monazite-(Ce) exhibits similar alteration features, which resulted in the formation of secondary fluorapatite, allanite-(Ce), a Th-U-Pb-Y-Ca silicate phase, and galena. In addition, minor replacement of primary monazite-(Ce) by fluorapatite occurred in the granite-hosted veins and in primary monazite-(Ce) in Olserum adjacent to these veins.

Stage C also includes Th+U alteration of xenotime-(Y) and, in part, monazite-(Ce). This alteration is manifested by different zoning patterns in xenotime-(Y) and monazite-(Ce) associated with various Th and U mineral inclusions. In monazite-(Ce), bright phases in back-scattered electron (BSE) images (mostly inclusions of various Th-U-Y-Ca silicates) are locally hosted within BSE-darker zones (low in Th, U, Si). In primary xenotime-(Y), thorite, uraninite, and minor monazite-(Ce) are present as inclusions in certain BSE-dark domains (e.g., Fig. 5B). Furthermore, BSE-bright Th-U-Y-Pb silicate phases are directly associated with BSE-dark zones, which are low in U ± Th ± REE ± Si and higher in Y. They occur adjacent to BSE-brighter zones, which are high in U ± Th ± REE ± Si and low in Y (Fig. 7A).

The primary (Fe,U,Y,REE,Ca,Si)-(Nb,Ta) oxide phase(s) were also affected by alteration. The altered phase is often porous and metamict, and occurs within magnetite, ilmenite, or biotite. The alteration assemblage varies slightly, but mostly comprises xenotime-(Y), columbite-(Fe), uraninite, galena, and monazite-(Ce). This alteration is locally manifested as discrete rims on the Nb-Ta oxide phase(s), which consists of columbite-(Fe) and xenotime-(Y) with minor galena and monazite-(Ce) (Fig. 7B).

Stage D. The youngest stage recognized is a widespread chloritization and martitization affecting all earlier assemblages. Magnetite is martitized most intensely in the BMS, in granite-hosted veins, and in assemblages in Djupedal, but also to a variable degree in Olserum. Moreover, magnetite is intermittently replaced by calcite and chlorite in Olserum, whereas in Djupedal, magnetite is mostly altered to chlorite only (e.g., Fig. 6D). Rutile replaces ilmenite, which invariably occurs within magnetite, whereas in Djupedal, in addition to rutile, minor titanite replaces ilmenite as well. Chloritization affected biotite from all assemblages, but to a greater extent in BMS and in Djupedal. REE mineral formation during this stage resulted from the alteration of allanite-(Ce) and ferriallanite-(Ce) to form chlorite and bastnäsite-(Ce) ± synchysite-(Ce) (Figs. 7C and 7D). All allanite generations experienced alteration, but only the allanite-(Ce) in BMS shows synchysite-(Ce) as one of the alteration products (Fig. 7D). Lastly, thin fracture-fillings of calcite crosscut the ore assemblages in both Olserum and Djupedal.

Mineral chemistry and trace element characteristics

Monazite-(Ce). All the different textural types of monazite-(Ce) occupy a rather small compositional range and only show small differences (Fig. 8A; Table EA3, Electronic Supplementary Material). Compared to primary monazite-(Ce) in Djupedal lacking alteration features, the pervasively altered monazite-(Ce) from Djupedal mostly has lower HREE+Y contents. Late-type monazite-(Ce) and BMS-related monazite-(Ce), which both exhibit incipient alteration along their grain margins, are however both still generally high in HREE+Y. BMS-related monazite-(Ce) also has elevated Th+U contents, with a predominance of Th over U. Fluorapatite-associated monazite-(Ce) is high in the middle rare earth elements (MREE) and typically also in Th+U. The cheralite ($\mathrm{Ca(Th,U,Pb)REE_{-2}}$) substitution mechanism (e.g., Förster 1998a) is generally important for most analyzed monazites (Fig. 8B). For some primary, distinctly zoned monazite-(Ce) in Olserum, the huttonite ($\mathrm{(Th,U,Pb)SiREE_{-1}P_{-1}}$) substitution mechanism is also important.

In normalized REE distribution diagrams (normalized to average upper continental crust; Rudnick and Gao 2003), all monazites exhibit similar patterns, characterized by high LREE, variable but low HREE contents, negative Eu anomaly, and a positive Y anomaly (Figs. 9A and B). The Eu anomaly is distinctly larger in monazite-(Ce) from Olserum compared to monazite-(Ce) from Djupedal. In terms of the $(\mathrm{La/Yb})_N$ ratio and calculated Eu anomaly (Eu/Eu*

$= Eu_N/0.5*(Sm_N+Gd_N)$), the pervasively altered monazite-(Ce) from Djupedal strongly differ from the other textural types, displaying higher $(La/Yb)_N$ and Eu/Eu* values (Fig. 10).

The trace elements always detected in monazite-(Ce) were V, Zr, Nb, and W, whereas S and Sc intermittently were below the limit of detection. Other trace elements such as Na, Ti, Cr, Mn, Ge, Sb, Ba, and Bi, which were included during initial LA-ICP-MS pilot testing, were below the limit of detection. Tantalum and Hf were mostly affected by interferences (see discussion in the Electronic Supplementary Material). When comparing the trace element compositions for the different types of monazite-(Ce), they are all rather similar with commonly low concentrations (Table EA4, Electronic Supplementary Material). Sulfur has the overall highest trace element concentrations measured, and is highest for primary monazite-(Ce) from Djupedal and monazite-(Ce) from the quartz-magnetite schlieren. The W content is comparably higher in late-type monazite-(Ce) than the other textural types.

Xenotime-(Y). Similar to monazite-(Ce), the major element compositional variation of xenotime-(Y) is rather limited (Fig. 11A; Table EA5, Electronic Supplementary Material). Fluorapatite-associated xenotime-(Y), and xenotime-(Y) related to the breakdown of primary (Fe,U,Y,REE,Ca,Si)-(Nb,Ta) oxide phase(s) both tend to have slightly higher LREE compared to most xenotimes. The latter type is also clearly higher in the HREE and lower in Y contents. The Th+U contents of xenotime-(Y) are also similar for most groups, except xenotime-(Y) from BMS and xenotime-(Y) related to the breakdown of Nb-Ta oxide phases. These typically exhibit higher Th+U contents, with a predominance of U over Th. In contrast to monazite-(Ce), the thorite substitution mechanism ($(Th,U,Pb)SiREE_{-1}P_{-1}$) in xenotime-(Y) is more important than the cheralite ($Ca(Th,U,Pb)REE_{-2}$) mechanism (Förster 1998b; Fig. 11B). However, the extent of substitution of Th and U in xenotime-(Y) is less significant than for monazite-(Ce).

Compositional zoning is much more prominent in xenotime-(Y) than in monazite-(Ce) and varies from slightly concentric or sector-like in primary xenotime-(Y) in the Djupedal mineralization (Fig. 5B), to very irregular (Fig. 7A) in both the Djupedal and Olserum mineralization. It is then often accompanied by thorite, uraninite or other U-Th-bearing phases. Generally, BSE-brighter zones are higher in Th+U or HREE or both, whereas BSE-darker zones are lower in Th+U and have high Y concentrations. In addition, BSE-darker zones intermittently contain slightly more LREE or less HREE. In rare cases, the zoning is due to differences in HREE versus LREE contents with no change in Y concentrations.

In normalized REE distribution diagrams (Figs. 12A and B), xenotime-(Y) from Olserum and Djupedal exhibit similar patterns with only minor differences. The difference is mostly manifested as contrasting Eu anomalies, where xenotime-(Y) from Olserum exhibits a larger Eu anomaly, whereas those from Djupedal invariably have a smaller Eu anomaly. Xenotime-(Y) exhibits a positive Y anomaly, except xenotime-(Y) related to the breakdown of Nb-Ta oxides, which has a small negative Y anomaly.

The trace elements V, Sc, Zr, Nb, Hf, and W were almost detected in xenotime-(Y), whereas S occasionally was below the limit of detection. The additional trace elements included during the LA-ICP-MS pilot runs were always below the limit of detection. Tantalum was mostly affected by interferences (see discussion in the Electronic Supplementary Material). Compared to monazite-(Ce), xenotime-(Y) contains higher concentrations of most of the trace elements, notably of Sc and Zr (Table EA6, Electronic Supplementary Material). The relative differences in trace element concentrations between the textural groups are minor, except for V, which is enriched in primary xenotime(Y) and monazite-(Ce) in Djupedal. The good correlation of Zr with Hf (Fig. 11C) probably indicates that both elements were incorporated into xenotime-(Y) via the same substitution mechanism. Together, Zr and Hf show a good correlation with either Si or Ca, or both.

Allanite-(Ce) and clinozoisite. Allanite and clinozoisite belong to the allanite and the epidote groups, respectively, of the epidote-supergroup of minerals. While allanite is one of the REE-bearing members of the allanite group, clinozoisite is an end-member with Al^{3+} being dominant in the octahedral M(3) site as compared to Fe^{3+} in the epidote end-member (Gieré and Sorensen 2004; Armbruster et al. 2006). Allanite is distinguished from ferriallanite by the M(1) site occupancy, where allanite contains predominantly Al^{3+} and ferriallanite Fe^{3+} (e.g., Gieré and Sorensen 2004). Massive and BMS-hosted allanite-(Ce) are similar in terms of their total REE contents, which are in the range of 21.2 – 28.5 and 21.4 – 27.8 wt% REE oxide, respectively (Table EA7, Electronic Supplementary Material). The replacement-type allanite-(Ce) has lower REE, ranging from 15.9 to 22.9 wt% REE oxide. The mineral-chemical variation of the epidote-group minerals is mainly governed by the following three substitutions: (1) $Ca^{2+} + Al^{3+} \leftrightarrow REE^{3+} + Fe^{2+}$, (2) $Ca^{2+} + Fe^{3+} \leftrightarrow REE^{3+} + Fe^{2+}$ and (3) $Fe^{3+} \leftrightarrow Al^{3+}$ (Petrík et al. 1995; Gieré and Sorensen 2004). These can be illustrated in a REE versus Al diagram (Fig. 13). The massive allanite-(Ce) as well as most of the replacement-type allanite-(Ce) plot along a line corresponding to substitution (1) where the data connect to the composition of the analyzed clinozoisite. The small shift relative to the ideal allanite-(Ce) composition is caused by substitutions (2) and (3). The allanite-(Ce) from BMS and a smaller population of the replacement-type allanite-(Ce) are richer in Fe^{3+}. This smaller subset of the replacement-type allanite-(Ce) has a calculated Fe^{3+} greater than 0.5 apfu, implying compositions ranging from allanite-(Ce) to ferriallanite-(Ce) (Armbruster et al., 2006). Moreover, the data show that all the replacement-type allanite-(Ce) to ferriallanite-(Ce) are richer in Ca than both BMS-related and massive allanite-(Ce) as a result of lower total REE contents occupying the A-site. The internal variations in $\sum$REE for each group reflect the zoning in allanite-(Ce) and ferriallanite-(Ce). Zones dark in BSE have lower LREE and higher Ca, and these zones typically host REE-fluorocarbonates. Clinozoisite has Ca contents close to the stoichiometric value of 2.0 apfu, and very low REE. The O(4) site is occupied by O, F, and other halogens. Measured F concentrations in the allanites vary from below the limit of detection (about 0.75 wt%), to about 1.0 wt% F, whereas Cl concentrations range from below the limit of detection (about 250 ppm) to a maximum of 3000 ppm Cl.

The normalized (relative to average upper continental crust; Rudnick and Gao 2003) REE distribution patterns of allanite-(Ce) and ferriallanite-(Ce) are similar to those of monazite-(Ce). They are characterized by higher LREE over HREE+Y, and negative Eu and Y anomalies (Fig. 14). Using the normalized ratios $(La/Yb)_N$ and $(La/Sm)_N$ and calculated Eu/Eu* and Y/Y* values ($Y/Y^* = Y_N/0.5^*(Dy_N+Ho_N)$), and looking at the sequence from BMS-hosted allanite-(Ce) to massive allanite-(Ce), to replacement-type allanite-(Ce) and ferriallanite-(Ce), the following trend emerges. Both the $(La/Yb)_N$ and Eu/Eu* systematically increase, while the $(La/Sm)_N$ and Y/Y* decrease (Figs. 14B to 13E). The BMS-hosted and massive allanite-(Ce) exhibit overlapping patterns with only very minor differences.

The trace element composition for the analyzed textural types of allanite differ from each other in most cases (Table EA8, Electronic Supplementary Material). The BMS-hosted allanite-(Ce) is strongly enriched in Zn and Sn and has slightly elevated Sc, V, and Ti concentrations. Massive allanite-(Ce) typically has low trace element concentrations, whereas replacement-type allanite-(Ce) and ferriallanite-(Ce) show variable concentrations, with moderately higher Sc, Mn, Th, and U contents. For Na, P, Sr, Ba, and Pb, the spread of individual analyses is larger and the quality of the LA-ICP-MS signals is rather poor, especially for BMS-hosted allanite-(Ce) and replacement-type allanite-(Ce) and ferriallanite-(Ce), which are subject to more extensive alteration and REE-fluorocarbonate formation. In addition to the elements always measured, initial tests showed the presence of low but variable concentrations of Co, Cr, Cs, In, Li, Mo, Nb, Ni, Rb, and Zr, while Be, Cd, Cu, and Tl were always below the limit of detection.

REE-fluorocarbonates. The REE-fluorocarbonates comprise a suite of chemically and structurally related minerals of which the most important are: bastnäsite ($REECO_3F$), parisite ($CaREE_2(CO_3)_3F_2$), röntgenite ($Ca_2REE_3(CO_3)_5F_3$), and synchysite ($CaREE(CO_3)_2F$). Since the grains of the REE-fluorocarbonates are typically rather small, only a limited set of analyses could be obtained, mainly from altered BMS-hosted allanite-(Ce) (Table EA7, Electronic Supplementary Material). Based on the EPMA data, two distinct phases are identified, namely bastnäsite-(Ce) with low Ca contents, ranging from 3.0 to 4.3 wt% CaO, and synchysite-(Ce), with higher Ca, varying between 14.1 and 18.6 wt% CaO. Both minerals are classified as fluorocarbonates with F dominant in the F-OH-Cl site (Fig. 15).

In a normalized (relative to average upper continental crust; Rudnick and Gao 2003) REE distribution diagram, bastnäsite-(Ce) and synchysite-(Ce) have slightly higher LREE and HREE compared to allanite-(Ce) (Fig. 14). The complete REE distribution pattern could only be obtained from two analyses of BMS-hosted bastnäsite-(Ce). These show similar Eu/Eu* and $(La/Yb)_N$ as their precursor BMS-hosted allanite-(Ce), but distinctly different Y/Y* and $(La/Sm)_N$ ratios. The trace element compositions of the analyzed bastnäsite-(Ce) show increased Sr, Th, and Fe contents (Table EA8, Electronic Supplementary Material).

Monazite-xenotime geothermometry

The temperature-dependent Y or Y+HREE partitioning between the equilibrium-pair monazite + xenotime (e.g., Heinrich et al. 1997; Pyle et al. 2001) has been utilized to provide temperature estimates for the formation of these minerals. Temperatures were calculated after the calibration of Pyle et al. (2001) on monazite-(Ce), using the combined EPMA (La-Sm) and LA-ICP-MS (Eu, Y, and Gd-Lu) data sets. Excluding grains that are not in physical contact with xenotime-(Y), the primary monazite-(Ce) from Olserum and Djupedal yield temperatures from c. 500 to 650 °C (Table 1). Monazite-(Ce) from granite-hosted veins shows overall slightly higher temperatures, similar to those of late-type and BMS-hosted monazite-(Ce). Monazite-(Ce) inclusions in fluorapatite on average exhibit higher temperatures compared to monazite-(Ce) in fractures and in the surrounding mineral matrix.

Discussion

Dissolution-reprecipitation processes

A mineral phase partly or completely replaced by the same phase or by another one can have formed as the result of fluid-assisted dissolution and concurrent precipitation. This process is initiated after the establishment of an interconnected pore space along the fluid-mineral interface, promoting the mass transfer of elements in the fluid (Putnis and John 2010). We suggest that such coupled dissolution-reprecipitation processes were important for the mineralogical and textural evolution of the Olserum-Djupedal mineralization (schematically illustrated in Fig. 4).

Similar to apatites from other REE-bearing deposits, for example several iron-oxide apatite deposits (e.g., Harlov et al. 2002, 2016; Jonsson et al. 2016, and references therein), primary fluorapatite and granite-hosted vein fluorapatite from the Olserum-Djupedal mineralization host abundant inclusions of monazite-(Ce) and xenotime-(Y), which we interpret to have formed by coupled dissolution-reprecipitation processes. Most of the monazite-(Ce) and xenotime-(Y) from Olserum-Djupedal are rich in Th or U or both, which is in contrast to most monazite-(Ce) and xenotime-(Y) formed by dissolution-reprecipitation (e.g., Harlov 2015, and references therein). Harlov and Förster (2003) experimentally demonstrated that monazite with high Th content could form from a fluorapatite host rich in Th, and that both Th and U are effectively liberated from fluorapatite at high P-T conditions in H_2O ± KCl rich fluids. However, fluorapatite from Olserum-Djupedal is low in both Th and U (Fullerton 2014; unpublished data; up to 3 ppm Th and up to 25 ppm U). An alternative explanation is that the infiltrating fluid carried both Th and U, and caused enrichment of both elements in the monazite-(Ce) and xenotime-(Y) inclusions.

The lack of inclusions along rims, in recrystallized grains and in zones parallel to fractures in the fluorapatite suggest that monazite-(Ce) and xenotime-(Y) inclusions formed early, and were affected by one or several subsequent stages of fluid-assisted remobilization. Monazite-(Ce), formed by remobilization, seems to occur further away, for instance in fractures in fluorapatite or within the surrounding matrix, whereas xenotime-(Y) tends to remain in fluorapatite as inclusions, typically as coarser grains probably grown by Ostwald ripening (Harlov et al. 2005). This contrasting behavior between monazite-(Ce) and xenotime-(Y) may be a direct consequence of the greater mobility of LREE compared to HREE, since LREE form more stable chloride complexes at hydrothermal conditions (e.g., Migdisov et al. 2009, 2016). A time-overlap is probable between monazite-(Ce) and xenotime-(Y) formed by these remobilization processes and those formed late during stage A. This is because all exhibit similar textural features, i.e., they are intergrown with magnetite (Figs. 5C and E), and they have a similar mineral chemistry. However, both monazite-(Ce) and xenotime-(Y) that formed late during stage A and those formed by processes associated with primary fluorapatite, experienced later dissolution-reprecipitation during stage C, which resulted in the formation of uraninite, thorite, and other Th-U-bearing phases.

Hetherington and Harlov (2008) demonstrated that dissolution-reprecipitation processes resulted in the formation of thorite and uraninite inclusions in xenotime-(Y) and monazite-(Ce) from granitic pegmatites in Norway. There, primary and unaltered xenotime-(Y) and monazite-(Ce) are rich in Si, Th ± U, i.e., high in huttonite/thorite components, whereas altered domains in these minerals are depleted in the same suite of elements. This implies essentially closed system conditions during the dissolution-reprecipitation process involving Th, U, and Si. In xenotime-(Y) from Olserum-Djupedal, smaller inclusions of thorite (with variable U, Y, Ca, and Pb contents) occur together with subordinate uraninite ± monazite-(Ce). These inclusions have precipitated in domains that make up the original crystal zoning (Fig. 5B), in domains exhibiting less distinct zoning patterns (Fig. 7A), or even in smaller fractures in xenotime-(Y). Comparable to the xenotime-(Y) from the granitic pegmatites in Norway (Hetherington and Harlov 2008), the altered, BSE-darker zones are depleted in Th+U, but they do also have higher Y and variable HREE and LREE contents. Conversely, the BSE-brighter zones are mainly enriched in Th + U ± Si, thus effectively demonstrating that similar dissolution-reprecipitation mechanisms operated here as well. However, the presence of small associated monazite-(Ce) grains also suggests that the dissolution-reprecipitation process liberated LREE from xenotime-(Y), which is consistent with the observed, strong LREE-depletion in some of the REE distribution patterns (Fig. 12). The prevalence of thorite over uraninite likely reflects the composition of the original unaltered xenotime-(Y) (Hetherington and Harlov 2008), resulting in Th/U < 1 in most of the (altered) xenotime-(Y) analyzed from Olserum-Djupedal.

The coupled dissolution-reprecipitation processes involving Th and U have less obviously affected monazite-(Ce). However, some monazite-(Ce) grains with a large huttonite component (e.g., Fig. 5A) exhibit unaltered BSE-bright zones enriched in Th and Si and BSE-darker zones. The latter are significantly depleted in Th and Si compared to the BSE-brighter zones, further demonstrating an essentially closed, or localized, chemical system. By contrast, monazite-(Ce) was more readily altered, pervasively or partially, to allanite-(Ce) and ferriallanite-

(Ce), fluorapatite, and clinozoisite (e.g., Figs. 6B and D). This resulted from fluid-assisted dissolution-reprecipitation initiated along grain boundaries or along fracture networks, which acted as pathways for fluids to migrate into and interact with monazite-(Ce). The process released REE that were incorporated into allanite-(Ce) and ferriallanite-(Ce), which typically formed directly on adjacent biotite, as the latter supplied the other major components Al, Si, Fe, and Mg. The required Ca may have been supplied either by: (1) the removal of Ca from primary fluorapatite that was affected by dissolution-reprecipitation processes or dissolved completely; (2) fluid-rock interaction with the surrounding host rocks; or (3) external sources, e.g., during regional Na ± Ca metasomatism of rocks in the Västervik formation (Hoeve 1974, 1978). The release of P from monazite-(Ce) and the readily available Ca in the reactive fluid caused the formation of the second generation of fluorapatite. Comparable monazite replacement textures in various igneous and metamorphic rocks (e.g., Broska and Siman 1998; Ondrejka et al. 2012; Budzyń and Jastrzêbski 2016) are usually interpreted as the result of fluid-rock interaction involving rocks with a granitic composition, where Ca originated from the anorthite component in plagioclase. However, we are unable to evaluate the extent of such an interaction in Olserum-Djupedal at this point, but note that the monazite-(Ce) alteration processes only occurred in Djupedal and in the biotite-magnetite schlieren, whose immediate surrounding is dominated by granite.

The pervasive replacement appears to have extensively modified the composition of the primary monazite-(Ce), which is depleted in HREE, exhibits lower Y/Y* ratios, and has a smaller Eu anomaly compared to the unaltered primary monazite-(Ce) in Djupedal. By contrast, partially altered monazite-(Ce) (late-type and BMS-hosted) exhibits only minor compositional changes. The excess HREE+Y liberated during the pervasive alteration were either incorporated into the newly formed fluorapatite, or more probably the late-type xenotime-(Y), which exhibits higher Y/Y*. The increase in Eu may reflect changes in oxidation state and Eu^{2+}/Eu^{3+} ratios during alteration (see discussion below). The depletion in the HREE+Y may also in part be explained by the precipitation of small xenotime-(Y) inclusions oriented along crystallographically controlled domains in the primary monazite-(Ce), as observed in both Olserum and Djupedal. The Th ± U released during pervasive or partial alteration of monazite-(Ce) led to the formation of discrete Th-bearing phases, if the monazite-(Ce) initially had high Th contents, or both elements were incorporated into allanite-(Ce) and ferriallanite-(Ce).

Temperature constraints

Based on geothermometry of texturally coexisting monazite-(Ce) and xenotime-(Y) pairs, the primary ore assemblages of stage A formed around 500-650 °C. Utilizing data from monazite-(Ce) that hosts small xenotime-(Y) inclusions, and from pervasively altered primary monazite-(Ce) from Djupedal, the calculated temperature range extends down to about 200 °C. We interpret the calculated lower end of the temperature range to reflect the fluid-mediated HREE+Y depletion in these monazites, rather than the true temperatures of formation. The temperatures calculated for monazite-(Ce) present as inclusions in fluorapatite are at the high end of the temperature spectrum, suggesting that the formation of these inclusions commenced at high temperatures. The subsequent fluid-assisted remobilization processes associated with fluorapatite operated under conditions where the hydrothermal system became progressively cooler. The lower temperatures, calculated for monazite-(Ce) formed by remobilization processes, are supported by the presence of coexisting biotite, andalusite, albite, quartz, and muscovite, which are readily interpreted as retrograde assemblages, formed at lower temperatures than the peak metamorphic mineral assemblages.

The presence of cordierite, andalusite, and staurolite in the ore assemblages is in good agreement with the temperature estimates obtained from monazite-xenotime thermometry.

The monazite-xenotime temperatures are also in good agreement with the broadly high-temperature, low-pressure conditions inferred for peak metamorphism in the Västervik area (e.g., Russel 1969; Kresten 1971; Gavelin 1984). Metamorphic conditions probably reached upper amphibolite facies (around 630-700 °C and <400 MPa), based on the presence of sillimanite + K-feldspar bearing assemblages (Elbers 1971; Kresten 1971). Sillimanite + K-feldspar assemblages have also been observed in the Olserum-Djupedal area, in sillimanite and K-feldspar gneisses, and pegmatite veins and schlieren, which are likely related to the peak metamorphic conditions attained in the region. In Djupedal, late-type monazite-(Ce), which has been affected by partial replacement along grain boundaries, nevertheless records relatively high temperatures (515-670 °C), and coexists with staurolite and quartz-muscovite symplectites (Fig. 6D). This demonstrates that the alteration of monazite-(Ce) likely occurred after these temperatures were reached, i.e., at slightly lower temperatures during retrograde conditions synchronous with the breakdown of K-feldspar. At such retrograde conditions, fluids with high Ca activity can still readily alter monazite to allanite or apatite or both (e.g., Spear 2010; Budzyń et al. 2011, 2016).

Fluid, mineral and textural evolution

Recent experimental studies addressing the solubility and speciation of the REE in aqueous solutions at hydrothermal conditions (e.g., Poitrasson et al. 2004; Migdisov et al. 2009, 2016; Loges et al. 2013; Tropper et al. 2013) have demonstrated that the REE can be efficiently transported under acidic conditions in chloride- and fluoride-rich fluids. However, the principal ore fluid at Olserum-Djupedal must have been capable of transporting the remaining elements of the primary mineralization stage A, most importantly Th, U, and Nb. One important common key factor appears to be the F content in the fluid, which greatly enhances the solubility of the REE and HFSE due to the formation of very stable metal-fluoride species (Keppler and Wyllie 1990, 1991; Jiang et al. 2005; Timofeev et al. 2015, 2017). Keppler and Wyllie (1990, 1991) showed that Cl-rich solutions are capable of transporting U, but not Th, and that the Th mobility increases with the F concentration in the system. Timofeev et al. (2015) and Timofeev et al. (2017) recently demonstrated that the solubility of both Nb and Ta increase with higher F concentration in the fluid. They also showed that Nb is one to two orders of magnitude more soluble than Ta under otherwise identical conditions (temperature, pressure, fluoride concentration, and pH). A plausible scenario is therefore that the primary REE-phosphate mineralization during stage A formed from fluids with elevated concentrations of both Cl and F compared to typical regional metamorphic fluids. The elevated F content in the system is inferred from the abundance of fluorapatite texturally coexisting with the monazite-(Ce) and xenotime-(Y). The ultimate source of the REE and HFSE transporting fluids for stage A remains a matter of speculation at this point, but the metamorphic assemblages and the close relation with the surrounding granite(s) would suggest fluid contributions from both metamorphic and magmatic sources to the hydrothermal REE mineralizing system.

The appearance of several Ca-bearing minerals during stage B and C, including allanite-(Ce) to ferriallanite-(Ce), clinozoisite, calcic tourmaline (uvite; unpublished data), and a second generation of fluorapatite, records an increase in the Ca content of the hydrothermal system. The Ca/Na activity ratio is a critical factor in controlling the stability of allanite over monazite (Spear 2010, Budzyń et al. 2011, 2016), in addition to the relative availabilities of P and Si. Indeed, massive allanite-(Ce) could only form locally together with the other Ca-rich minerals during stage B. Moreover, all late-type monazite-(Ce), formed together with massive allanite-(Ce) in Ca-rich assemblages, was evidently unstable during later monazite-(Ce) alteration. The transition from massive allanite-(Ce) (stage B) to replacement-type allanite-(Ce) and ferriallanite-(Ce) (stage C) records an increase in the Ca content, which further attest to an increase in Ca in the system. Whether this increase reflects the local fluid-rock interaction with surrounding Ca-rich host rocks or external introduction of Ca into the system cannot be resolved at present. In Olserum, where no allanite formed and monazite-(Ce) essentially lacks alteration, no other Ca-bearing minerals were formed during stages B and C.

It is not yet fully clear why this localized hydrothermal alteration developed in Djupedal and not in Olserum, but a first-order observation is the distinct difference in the immediate host-rock lithology, i.e., more granitic rocks in Djupedal compared to mainly metasedimentary rocks at Olserum. In addition to high Ca activity, local differences in the Eu/Eu* of monazite-(Ce) between the Olserum mineralization, the Djupedal mineralization, and the REE mineralization in BMS suggest that differences in oxidation appear to be another factor controlling the stability of monazite-(Ce) (Fig. 10). In principle, monazite-(Ce) preferably incorporates trivalent REE ions. If monazite-(Ce) formed from a fluid with dominantly Eu^{3+}, no Eu anomaly would develop. When the fluid becomes reduced so that Eu^{2+} dominates, less Eu^{3+} is then available for monazite-(Ce) and a negative anomaly develops. However, we do not necessarily attribute the overall negative Eu anomaly in monazite-(Ce), and the other REE minerals, to the presence of a reducing fluid. Instead, we interpret this mainly as a result of inheritance in the source region via fluid-rock interactions. This is because both metasedimentary rocks and granitoids from the Västervik area invariably exhibit negative Eu anomalies (Nolte et al. 2011; Kleinhanns et al. 2012). Yet, the relative increase in Eu/Eu* values, i.e., progressively smaller Eu anomalies, from the unaltered to the pervasively altered monazite-(Ce) in Djupedal, suggest a progressive oxidation of the fluid during this alteration. This is because oxidized Eu^{3+} should dominate over reduced Eu^{2+} in an oxidizing fluid, and become more available for monazite-(Ce). This eventually produces progressively smaller negative Eu anomalies. The inferred increase in oxidation is also supported by the relative increase in Fe^{3+} over Fe^{2+} and in Eu/Eu* (Figs. 10 and 13) from massive allanite-(Ce) to the replacement-type allanite-(Ce) and ferriallanite-(Ce) (from stage B to C). Additionally, widespread martitization of magnetite during stage D, or potentially earlier, corroborates with this progressive oxidation of the system.

In addition to the pervasive or partial alteration of monazite-(Ce), stage C records additional secondary, fluid-assisted alteration, and replacement processes. Experimental studies investigating similar processes have demonstrated that in the presence of F- and alkali-bearing fluids at temperatures between 450 and 750 °C (and at pressures between 200 and 1000 MPa), monazite and xenotime are highly reactive (Hetherington et al. 2010; Budzyń et al. 2011, 2016; Harlov et al. 2011). Experiments involving xenotime-(Y) produced breakdown of the xenotime to (Y,HREE)-epidote or Y-rich fluorcalciobritholite, coupled with a Th ± U alteration (Hetherington et al. 2010; Budzyń et al. 2016). This contrasts with the observations from ore textures and minerals assemblages in Olserum-Djupedal, where xenotime-(Y) shows no indication of (Y,HREE)-epidote alteration. The lack of such alteration may reflect different temperature and pressure conditions, or more likely the result of lower fluid-rock ratios compared to the conditions of the experiments of Budzyń et al. (2016). The breakdown of the primary (Y,REE,U,Fe)-(Nb-Ta) oxide phases may also have been induced by Cl- and F-bearing fluids, as suggested by the study of alteration textures of primary euxenite in pegmatites in southern Norway (Duran et al. 2016).

While an alkali-bearing fluid promotes dissolution-reprecipitation processes in monazite-(Ce) and xenotime-(Y), such a fluid will not cause the formation of monazite-(Ce) and xenotime-(Y) inclusions in fluorapatite (Harlov and Förster 2003; Harlov et al. 2005). This process would rather be facilitated by H_2O-KCl brines and CO_2-H_2O fluids (Harlov and Förster 2003) and acids such as HCl and H_2SO_4 (Harlov et al. 2005). Conversely, similar fluid compositions will not cause the Th + U alteration in monazite-(Ce) and xenotime-(Y), and the partial to pervasive replacement of monazite-(Ce) (Budzyń et al. 2011). Hence, the coupled dissolution-reprecipitation processes affecting monazite-(Ce), xenotime-(Y), and the (Y,REE,U,Fe)-(Nb-Ta) oxide phases (stage C), as opposed to the processes affecting fluorapatite (stage B), require a different type of fluid chemistry. Thus, textural observations combined with the inferences from experimental studies suggest that these two alteration types were produced at distinctly separate stages and driven by chemically different fluids. Textural relations show that coarsened xenotime-(Y) grains located at fluorapatite grain boundaries exhibit the same type of Th ± U alteration as the primary xenotime-(Y). This implies that the precipitation of monazite-(Ce) and xenotime-(Y) inclusions in fluorapatite preceded the Th ± U alteration of stage C, and, by implication, also the alteration affecting monazite-(Ce).

Stage D represents the latest stage of REE mineral formation. This stage comprises the REE-fluorocarbonates bastnäsite-(Ce) and synchysite-(Ce). They formed as a consequence of low-temperature alteration of allanite-(Ce) and ferriallanite-(Ce) that proceeded along fractures or grain boundaries, or sometimes in intragranular domains. REE released from the allanites became incorporated into the REE-fluorocarbonates, while excess Al, Si, Fe, and Mg liberated during the alteration formed chlorite. If the alteration was unable to affect the entire grain, the Al, Si, Fe, and Mg, together with the REE, intermittently remained in allanite, resulting in BSE-darker zones that contain thin fracture fillings of bastnäsite-(Ce). The liberated Th ± U was probably incorporated into the REE-fluorocarbonates, as shown by measurable Th and minor U contents in these phases. However, U also formed discrete uraninite grains close to the altered allanite (Fig. 7D). The F required to stabilize REE-fluorocarbonates was most likely derived from the chloritization of biotite, or from the external fluid. In the allanite-bearing assemblages in Djupedal, which experienced extensive chloritization, magnetite also became chloritized. In contrast, magnetite in Olserum was only altered to calcite + chlorite. Thus, late chloritization and influx of CO_2 ± F caused the formation of REE-fluorocarbonates in those domains of the mineralization rich in allanite-(Ce) or ferriallanite-(Ce), whereas calcite formed instead in domains lacking allanite.

Implications

The present study describes a new and previously unrecognized type of potentially economic hydrothermal REE mineralization dominated by abundant, coarse-grained monazite-(Ce), xenotime-(Y), and fluorapatite. The abundance of these phosphates clearly shows that the REE mineralizing system contained P as one of its principal components. Currently, phosphate is generally assumed to act as a precipitant rather than a complexing ligand for REE in hydrothermal systems, reflecting the low solubility of REE-phosphates at typical low- to moderate-temperature hydrothermal conditions (Poitrasson et al. 2004; Cetiner et al. 2005; Gysi et al. 2015; Migdisov et al. 2016). However, because of the strong enrichment of REE-phosphates in the Olserum-Djupedal mineralization, mass balance considerations suggest that the REE-transporting fluid must have locally interacted with substantial volumes of P-enriched host rocks in order to precipitate REE exclusively as phosphates. Considering that the REE-phosphates formed concomitantly with vein-hosted fluorapatite (instead of post-dating it), and that no other P-enriched units or earlier assemblages have been identified, a local rock source for the necessary, large amounts of P remains problematic. In addition, the Olserum-Djupedal REE mineralization formed at rather high P-T conditions, which are above the P-T ranges normally investigated by solubility and spectroscopic experiments. Thus, the possibilities that the REE can be cotransported with phosphate in F-rich fluids or even form stable phosphate complexes at such conditions calls for new experimental studies at high P-T conditions.

The REE-bearing hydrothermal ore assemblages of the Olserum-Djupedal mineralization further demonstrate the joint mobility of REE and HFSE in a natural F-bearing, high-temperature hydrothermal system, both during the primary stage of formation, and the subsequent alteration stages that modified the primary REE-phosphate ores. Similar to the conclusions drawn in other studies (e.g., Williams et al. 2011), we suggest that the fluid-assisted metasomatic processes in the Olserum-Djupedal mineralization have extensively altered the mineral assemblages and composition in some cases (i.e., during the Th ± U alteration or the pervasive monazite replacement), whereas in other cases the original mineralogy and chemical composition remained essentially unchanged. Consequently, if these textures and chemical variations are mapped in sufficient detail, geochronological dating could be applied to monazite and xenotime in systems where the primary age and the subsequent alteration stages are expected to be larger than the error for the selected dating method.

Acknowledgments

This study was made possible by funding to S.S.A. from the GeoDoc Graduate Program (Graduate School, Faculty of Sciences, University of Helsinki) and complementary funding to T.W. from the Academy of Finland (project number 280458). E.J. acknowledges support from the Swedish Research Council (Vetenskapsrådet) to Uppsala University, and from the Geological Survey of Sweden (SGU). The outstanding support from Tasman Metals, and in particular from Magnus Leijd and Johan Berg during field work, is greatly acknowledged. We thank Helena Korkka for the preparation of polished thin sections, and Tobias Fusswinkel for assistance with LA-ICP-MS analysis. Daniel Harlov (GFZ Potsdam, Germany) generously provided synthetic REE- and Y-phosphate standards for EPMA analysis, which is greatly appreciated. We thank Sam Broom-Fendley and Daniel Harlov for their constructive reviews, which helped to improve the manuscript.

References cited

Åhäll, K.I., and Larson, S.A. (2000) Growth-related 1.85-1.55 Ga magmatism in the Baltic Shield; a review addressing the tectonic characteristics of Svecofennian, TIB 1-related, and Gothian events. GFF, 122, 193-206.

Andersen, T. (1984) Secondary processes in carbonatites: petrology of “rødberg” (hematite-calcite-dolomite carbonatite) in the Fen central complex, Telemark (South Norway). Lithos, 17, 227-245.

Andersen, T. (1986) Compositional variation of some rare earth minerals from the Fen complex (Telemark, SE Norway): implications for the mobility of rare earths in a carbonatite system. Mineralogical Magazine, 50, 503-509.

Andersen, T., Andersson, U.B., Graham, S., Åberg, G., and Simonsen, S.L. (2009) Granitic magmatism by melting of juvenile continental crust: new constraints on the source of Palaeoproterozoic granitoids in Fennoscandia from Hf isotopes in zircon. Journal of the Geological Society, London, 166, 233-247.

Andersson, U.B., and Wikström, A. (2004) The Småland-Värmland Belt - Overview. In K. Högdahl, U.B. Andersson, and O. Eklund, Eds., The Transscandinavian Igneous Belt (TIB) in Sweden: A Review of Its Character and Evolution. Geological Survey of Finland Special Paper, 37, 16-20.

Armbruster, T., Bonazzi, P., Akasaka, M., Bermanec, V., Chopin, C., Gieré, R. Heuss-Assbichler, S., Liebscher, A., Manchetti, S., Pan, Y., and Pasero, M. (2006) Recommended nomenclature of epidote-group minerals. European Journal of Mineralogy, 18, 551-567.

Beunk, F.F., and Page, L.M. (2001) Structural evolution of the accretional continental margin of the Paleoproterozoic Svecofennian orogen in southern Sweden. Tectonophysics, 339, 67-92.

Billström, K., Broman, C., and Söderhielm, J. (2004) The Solstad Cu ore - an Fe oxide-Cu-Au type deposit in SE Sweden. GFF 126, 147-148.

Broom-Fendley, S., Brady, A.E., Wall, F., Gunn, G., and Dawes, W. (2017) REE minerals at the Songwe Hill carbonatite, Malawi: HREE-enrichment in late-stage apatite. Ore Geology Reviews, 81, 23-41.

Broska, I., and Siman, P. (1998) The breakdown of monazite in the West-Carpathian Veporic orthogneisses and Tatric granites. Geologica Carpathica, 49, 161-167.

Budzyń, B., Harlov, D.E., Williams, M.L., and Jercinovic, M.J. (2011) Experimental determination of stability relations between monazite, fluorapatite, allanite, and REE-epidote as a function of pressure, temperature, and fluid composition. American Mineralogist, 96, 1547-1567.

Budzyń, B., Harlov, D.E., Kozub-Budzyń, G., and Majka, J. (2016) Experimental constraints on the relative stabilities of the two systems monazite-(Ce) – allanite-(Ce) – fluorapatite and xenotime – (Y) – (Y,HREE)-rich epidote – (Y,HREE)-rich fluorapatite, in high Ca and Na-Ca environments under P-T conditions of 200–1000 MPa and 450–750 °C. Mineralogy and Petrology, 1-35.

Budzyń, B., and Jastrzêbski, M. (2016) Monazite stability and the maintenance of Th-U-total Pb ages during post-magmatic processes in granitoids and host metasedimentary rocks: a case study from the Sudetes (SW Poland). Geological Quarterly, 60, 104-121.

Cetiner, Z., Wood, S.A., and Gammons, C.H. (2005) The aqueous geochemistry of the rare earth elements. Part XIV. The solubility of rare earth element phosphates from 23 to 150 °C. Chemical Geology, 217, 147-169.

Chakhmouradian, A.R., and Zaitsev, A.N. (2012) Rare earth mineralization in igneous rocks: Sources and processes. Elements, 8, 347-353.

Chao, E.C.T., Back, J.M., and Minkin, J.A. (1992) Host-rock controlled epigenetic, hydrothermal metasomatic origin of the Bayan Obo REE-Fe-Nb ore deposit, Inner Mongolia, P.R.C. Applied Geochemistry, 7, 443-458.

Cook, N.J., Ciobanu, C.L., O'Reilly, D., Wilson, R., Das, K., and Wade, B. (2013) Mineral chemistry of rare earth element (REE) mineralization, Browns Ranges, Western Australia. Lithos, 172-173, 192-213.

Djenchuraeva, R.D., Borisov, F.I., Pak, N.T., and Malyukova, N.N. (2008) Metallogeny and geodynamics of the Aktiuz–Boordu mining district, northern Tien Shan, Kyrgyzstan. Journal of Asian Earth Sciences, 32, 280-299.

Duran, C.J., Seydoux-Guillaume, A.-M., Bingen, B., Gouy, S., de Parseval, P., Ingrin, J., and Guillaume, D. (2016) Fluid-mediated alteration of (Y,REE,U,Th)–(Nb,Ta,Ti) oxide minerals in granitic pegmatite from the Evje-Iveland district, southern Norway. Mineralogy and Petrology, 110, 581-599.

Elbers, F.J. (1971) Evolution of the Svecofennian orogeny in the northeastern part of the Västervik area, southeastern Sweden, with special reference to deformation, metamorphism and magmatism. Ph.D. thesis, Vrije University, Amsterdam, 56 p.

Förster, H.J. (1998a) The chemical composition of REE-Y-Th-U-rich accessory minerals from peraluminous granites of the Erzgebirge–Fichtelgebirge region, Germany, Part I: The monazite-(Ce) – brabantite solid solution series. American Mineralogist, 83, 259-272.

Förster, H.J. (1998b) The chemical composition of REE-Y-Th-U-rich accessory minerals from peraluminous granites of the Erzgebirge–Fichtelgebirge region, Germany. Part II: Xenotime. American Mineralogist, 83, 1302-1315.

Fullerton, W. (2014) REE mineralisation and metasomatic alteration in the Olserum metasediments. Master thesis, Lund University, Lund, 86 p.

Gaál, G., and Gorbatschev, R. (1987) An outline of the Precambrian evolution of the Baltic shield. Precambrian Research, 35, 15-52.

Gavelin, S. (1984) The Västervik area in south-eastern Sweden. Studies in Proterozoic sedimentation, high-grade metamorphism and granitization. Sveriges Geologiska Undersökning, Ba 32, 172 p.

Gieré, R., and Sorensen, S.S. (2004) Allanite and other REE-Rich Epidote-Group Minerals. Reviews in Mineralogy and Geochemistry, 56, 431-493.

Goodenough, K.M., Schilling, J., Jonsson, E., Kalvig, P., Charles, N., Tuduri, J., Deady, E.A., Sadeghi, M., Schiellerup, H., Müller, A., Bertrand, G., Arvanitidis, N., Eliopolous, D.G., Shaw, R. A., Thrane, K., and Keulen, N. (2016) Europe´s rare earth element resource potential: an overview of metallogenetic provinces and their geodynamic setting. Ore Geology Reviews, 72, 838-856.

Guillong, M., Meier, D.L., Allan, M.M., Heinrich, C.A., Yardley, B.W.D. (2008) SILLS: a MATLAB-based program for the reduction of laser ablation ICP-MS data of homogeneous materials and inclusions. Mineralogical association of Canada, Short Course, 40, 328–333.

Gysi, A.P., Williams-Jones, A.E., and Harlov, D. (2015) The solubility of xenotime-(Y) and other HREE phosphates ($DyPO_4$, $ErPO_4$ and $YbPO_4$) in aqueous solutions from 100 to 250 °C and psat. Chemical Geology, 401, 83-95.

Gysi, A.P., Williams-Jones, A.E., and Collins, P. (2016) Lithogeochemical vectors for hydrothermal processes in the Strange Lake peralkaline granitic REE-Zr-Nb deposit. Economic Geology, 111, 1241-1276.

Harlov, D.E. (2015) Apatite: A fingerprint for metasomatic processes. Elements, 11, 171-176.

Harlov, D.E., and Förster, H.J. (2003) Fluid-induced nucleation of (Y+REE)-phosphate minerals within fluorapatite: Nature and experiment. Part II. Fluorapatite. American Mineralogist, 88, 1209-1229.

Harlov, D.E., Andersson, U.B., Förster, H.J., Nyström, J.O., Dulski, P., and Broman, C. (2002) Fluorapatite-monazite relations in the Kiirunavaara magnetite-fluorapatite ore, northern Sweden. Chemical Geology, 191, 47-72.

Harlov, D.E., Wirth, R., and Förster, H.J. (2005) An experimental study of dissolution-reprecipitation in fluorapatite: Fluid infiltration and the formation of monazite. Contributions to Mineralogy and Petrology, 150, 268-286.

Harlov, D.E., Wirth, R., and Hetherington, C.J. (2011). Fluid-mediated partial alteration in monazite: the role of coupled dissolution–reprecipitation in element redistribution and mass transfer. Contributions to Mineralogy and Petrology, 162, 329-348.

Harlov, D.E., Meighan, C., Kerr, I., and Samson, I.M. (2016) Mineralogy, chemistry, and fluid-aided evolution of the Pea Ridge Fe-oxide-REE deposit, southeast Missouri, USA. Economic Geology, 111, 1963-1984.

Heinrich, W., Andrehs, G., and Franz, G. (1997) Monazite–xenotime miscibility gap thermometry: I. An empirical calibration. Journal of Metamorphic Geology, 15, 3-17.

Hetherington, C.J., and Harlov, D.E. (2008) Metasomatic thorite and uraninite inclusions in xenotime and monazite from granitic pegmatites, Hidra anorthosite massif, southwestern Norway: mechanics and fluid chemistry. American Mineralogist, 93, 806-820.

Hetherington, C.J., Harlov, D.E., and Budzyń, B. (2010) Experimental initiation of dissolution-reprecipitation reactions in monazite and xenotime: the role of fluid composition. Mineralogy and Petrology, 99, 165-184.

Hoeve, J. (1974) Soda metasomatism and radio-active mineralisation in the Västervik area, southeastern Sweden. Ph.D. thesis, Vrije University, Amsterdam, 191 p.

Hoeve, J. (1978) Composition and volume changes accompanying soda metasomatic alterations, Västervik area, SE Sweden. Geologische Rundschau, 67, 920-942.

Högdahl, K., Andersson, U. B., and Eklund, O. (eds.). (2004) The Transscandinavian Igneous Belt (TIB) in Sweden: a review of its character and evolution. Geological Survey of Finland Special Paper, 37, 125 p.

Jiang, SY., Wang, R.C., Xu, X.S., and Zhao, K.D. (2005) Mobility of high field strength elements (HFSE) in magmatic-, metamorphic-, and submarine-hydrothermal systems. Physics and Chemistry of the Earth, 30, 1020-1029.

Jonsson, E., Harlov, D.E., Majka, J., Högdahl, K., and Person-Nilsson, K. (2016) Fluorapatite-monazite-allanite relations in the Grängesberg apatite-iron oxide ore district, Bergslagen, Sweden. American Mineralogist, 101, 1769-1782.

Keppler, H., and Wyllie, P.J. (1990) Role of fluids in transport and fractionation of uranium and thorium in magmatic processes. Nature, 348, 531-533.

Keppler, H., and Wyllie, P.J. (1991) Partitioning of Cu, Sn, Mo, W, U and Th between melt and aqueous fluid in the system haplogranite-H_2O-HCl and haplogranite-H_2O-HF. Contributions to Mineralogy and Petrology, 109, 139-150.

Kleinhanns, I.C., Fischer-Goedde, M., and Hansen, B.T. (2012) Sr–Nd isotope and geochemical characterisation of the Paleoproterozoic Västervik formation (Baltic Shield, SE Sweden): a southerly exposure of Svecofennian metasiliciclastic sediments. International Journal of Earth Sciences, 101, 39-55.

Kleinhanns, I.C., Whitehouse, M.J., Nolte, N., Baero, W., Wilsky, F., Hansen, B.T., and Schoenberg, R. (2015) Mode and timing of granitoid magmatism in the Västervik area (SE

Sweden, Baltic Shield): Sr–Nd isotope and SIMS U–Pb age constraints. Lithos, 212-215, 321-337.

Korja, A., Lahtinen, R., and Nironen, M. (2006) The Svecofennian orogen: a collapse of microcontinents and island arcs. In: Gee, D.G. & Stephenson, R.A. (eds.): European Lithosphere Dynamics. Geological Society of London Memoirs, 32, 561-578.

Kresten, P. (1971). Metamorphism and migmatization in the Västervik area, SE Sweden. Geologiska Föreningen i Stockholm Förhandlingar, 93, 743-764.

Kresten, P. (1986) The Granites of the Västervik Area, South-Eastern Sweden. Sveriges Geologiska Undersökning, C 814, 35 p.

Lahtinen, R., Korja, A., Nironen M., and Heikkinen, P. (2009) Palaeoproterozoic accretionary processes in Fennoscandia. In. P.A. Cawood and A. Kröner, Eds., Earth Accretionary Systems in Space and Time. Geological Society, Special publications, London, 318, p. 237-256.

Loges, A., Migdisov, A.A., Wagner, T., Williams-Jones, A.E., and Markl, G. (2013) An experimental study of the aqueous solubility and speciation of Y(III) fluoride at temperatures up to 250 °C. Geochimica et Cosmochimica Acta, 123, 403-415.

McKinney, S.T., Cottle, J.M., and Lederer, G.W. (2015) Evaluating rare earth element (REE) mineralization mechanisms in Proterozoic gneiss, Music Valley, California. Geological Society of America Bulletin, 127, 1135-1152.

Migdisov, A.A., Williams-Jones, A.E., and Wagner, T. (2009) An experimental study of the solubility and speciation of the Rare Earth Elements (III) in fluoride- and chloride-bearing aqueous solutions at temperatures up to 300°C. Geochimica et Cosmochimica Acta, 73, 7087-7109.

Migdisov, A.A., Williams-Jones, A.E., van Hinsberg, V., and Salvi, S. (2011) An experimental study of the solubility of baddeleyite (ZrO_2) in fluoride-bearing solutions at elevated temperature. Geochimica et Cosmochimica Acta, 75, 7426-7434.

Migdisov, A., Williams-Jones, A.E., Brugger, J., and Caporuscio, F.A. (2016) Hydrothermal transport, deposition, and fractionation of the REE: Experimental data and thermodynamic calculations. Chemical Geology, 439, 13-42.

Nironen, M. (1997) The Svecofennian Orogen: a tectonic model. Precambrian Research, 86, 21-44.

Nolte, N., Kleinhanns, I.C., Baero, W., and Hansen, B.T. (2011) Petrography and whole-rock geochemical characteristics of Västervik granitoids to syenitoids, southeast Sweden: constraints on petrogenesis and tectonic setting at the southern margin of the Svecofennian domain. GFF, 133, 173-194.

Ondrejka, M., Uher, P., Putiš, M., Broska, I., Bačík, P., Konečný, P., and Schmiedt, I. (2012) Two-stage breakdown of monazite by post-magmatic and metamorphic fluids: an example from the Veporic orthogneiss, Western Carpathians, Slovakia. Lithos, 142–143, 245-255.

Petrík, I., Broska, I., Lipka, J., and Siman, P. (1995) Granitoid allanite-(Ce) substitution relations, redox conditions and REE distributions (on an example of I-type granitoids, western Carpathians, Slovakia). Geologica Carpathica, 46, 79-94.

Poitrasson, F., Oelkers, E., Schott, J., and Montel, J.M. (2004) Experimental determination of synthetic $NdPO_4$ monazite end-member solubility in water from 21 °C to 300 °C: Implications for rare earth element mobility in crustal fluids. Geochimica et Cosmochimica Acta, 68, 2207-2221.

Putnis, A., and John, T. (2010) Replacement processes in the Earth's crust. Elements, 6, 159-164.

Pyle, J.M., Spear, F.S., Rudnick, R.L., and McDonough, W.F. (2001) Monazite–xenotime–garnet equilibrium in metapelites and a new monazite–garnet thermometer. Journal of Petrology, 42, 2083-2107.

Pyle, J.M., Spear, F.S., and Wark, D.A. (2002) Electron microprobe analysis of REE in apatite, monazite and xenotime: Protocols and pitfalls. Reviews in Mineralogy and Geochemistry, 48, 337-362.

Reed, G.C. (2013) Amended and restated technical report for Olserum REE deposit, southern Sweden. Tasman Metals, Vancouver.

Rudnick, R.L., and Gao, S. (2003) Composition of the continental crust. Treatise on Geochemistry, 3, 1-64.

Russel, R. (1969) Porphyroblastic differentiation in fleck gneiss from Västervik, Sweden. Geologiska Föreningen i Stockholm Förhandlingar, 91, 217-282.

Salvi, S., and Williams-Jones, A. E. (1990) The role of hydrothermal processes in the granite hosted Zr, Y, REE deposit at Strange Lake, Quebec/Labrador: Evidence from fluid inclusions. Geochimica et Cosmochimica Acta, 54, 2403-2418.

Smith, M., and Henderson, P. (2000) Preliminary fluid inclusion constraints on fluid evolution in the Bayan Obo Fe-REE-Nb deposit, Inner Mongolia, China. Economic Geology, 95, 1371-1388.

Smith, M.P., Campbell, L.S., and Kynicky, J. (2015) A review of the genesis of the world class Bayan Obo Fe-REE-Nb deposits, Inner Mongolia, China: Multistage processes and outstanding questions. Ore Geology Reviews, 64, 459-476.

Spandler, C., Pettke, T., and Rubatto, D. (2011) Internal and external fluid sources for eclogite facies veins in the Monviso meta-ophiolite, Western Alps: implications for fluid flow in subduction zones. Journal of Petrology, 52, 1207-1236.

Spear, F.S. (2010) Monazite–allanite phase relations in metapelites. Chemical Geology, 279, 55-62.

Stephens, M.B., Ripa, M., Lundström, I., Persson, L., Bergman, T., Ahl, M., Wahlgren, C.H., Persson, P.O., and Wickström, L. (2009) Synthesis of the bedrock geology in the Bergslagen region, Fennoscandian Shield, south-central Sweden. Sveriges Geologiska Undersökning, Ba 58, 260 p.

Sultan, L., Claesson, S., and Plink-Björklund, P. (2005) Proterozoic and Archaean ages of detrital zircon from the Palaeoproterozoic Västervik Basin, SE Sweden: implications for provenance and timing of deposition. GFF, 127, 17-24.

Sundblad, K. (2003) Metallogeny of gold in the Precambrian of northern Europe. Economic Geology 98, 1271-1290.

Timofeev, A., Migdisov, A.A., and Williams-Jones, A.E. (2015) An experimental study of the solubility and speciation of niobium in fluoride-bearing aqueous solutions at elevated temperature. Geochimica et Cosmochimica Acta, 158, 103-111.

Timofeev, A., Migdisov, A.A., and Williams-Jones, A.E. (2017) An experimental study of the solubility and speciation of tantalum in fluoride-bearing aqueous solutions at elevated temperature. Geochimica et Cosmochimica Acta, 197, 294-304.

Tropper, P., Manning, C.E., and Harlov, D.E. (2013) Experimental determination of $CePO_4$ and YPO_4 solubilities in H_2O–NaF at 800°C and 1 GPa: implications for rare earth element transport in high-grade metamorphic fluids. Geofluids, 13, 372-380.

Uytenbogaardt, W. (1960) Uranium mineralization in the Västervik area. In: A. Noe-Nygaard, T. Siggerud, and O. Vaasjoki, Eds., Report of the 21st session International Geological Congress Norden, Genetic problems of uranium and thorium deposits, 15, 114-122. The 21st International Geological Congress, Norden, Copenhagen.

Wall, F., and Mariano, A.N. (1996) Rare earth minerals in carbonatites: a discussion centred on the Kangankunde carbonatite, Malawi. In. A.P. Jones, F. Wall, and C.T. Williams, Eds., Rare earth minerals: Chemistry, origin and ore deposits. Mineralogical society, 7, 193-225.

Wall, F., Niku-Paavola, V.N., Storey, C., Müller, A., and Jeffries, T. (2008) Xenotime-(Y) from carbonatite dykes at Lofdal, Namibia: Unusually low LREE:HREE ratio in carbonatite, and the first dating of xenotime overgrowths on zircon. The Canadian Mineralogist, 46, 861-877.

Welin, E., and Uytenbogaardt, W. (1963) Notes on the mineralogy of Sweden. 3. A davidite–thorite paragenesis on the island of Björkö, north of Västervik, Sweden. Arkiv för Kemi, Mineralogi och Geologi, 3, 277-292.

Welin, E. (1966a) Uranium Mineralizations and age Relationships in the Precambrian Bedrock of Central and Southeastern Sweden. Geologiska Föreningen i Stockholm Förhandlingar, 88, 34-67.

Welin, E. (1966b) Two occurrences of uranium in Sweden – the Los cobalt deposit and the iron ores of the Västervik area. Geologiska Föreningen i Stockholm Förhandlingar, 87, 492-508.

Williams, M.L., Jercinovic, M.J., Harlov, D.E., Budzyń, B., and Hetherington, C.J. (2011) Resetting monazite ages during fluid-related alteration. Chemical Geology, 283, 218-225.

Williams-Jones, A.E., Samson, I.M., and Olivo, G.R. (2000) The genesis of hydrothermal fluorite-REE deposits in the Gallinas Mountains, New Mexico. Economic Geology, 95, 327-341.

Figure captions

Figure 1. Geological map of the Västervik area showing the location of the Olserum-Djupedal REE deposits. Redrawn after Gavelin (1984) and mapping data from the database of the Geological Survey of Sweden. The inset map shows the large-scale geology of southern Sweden, modified after Andersen et al. (2009).

Figure 2. Overview of the ore assemblages of the Olserum–Djupedal REE mineralization. **(A)** Biotite-dominated vein with magnetite, fluorapatite, xenotime-(Y), and monazite-(Ce), in metasedimentary quartz-biotite rock. The REE vein is crosscut by a calcite fracture. **(B)** Irregular biotite vein with coarse-grained monazite-(Ce) and xenotime-(Y) in metasedimentary quartz-biotite rock. **(C)** Intergrown magnetite, monazite-(Ce), xenotime-(Y), and fluorapatite in a K-feldspar rich granite, surrounded by a weak alteration halo of quartz, biotite, muscovite, and albitized K-feldspar. **(D)** Allanite-(Ce) bearing assemblages in the ore at Djupedal. Coarse-grained and fractured monazite-(Ce) and xenotime-(Y) occur in a matrix dominated by biotite, quartz, cordierite, and muscovite.

Figure 3. Simplified paragenesis diagram of the Olserum-Djupedal REE mineralization, illustrating the relative time sequence of the REE-Th-U-Nb minerals and the main gangue and alteration minerals.

Figure 4. Schematic illustration showing the textural evolution of the REE minerals and the difference between Olserum, Djupedal, and the biotite-magnetite schlieren.

Figure 5. BSE images of ore assemblages from the Olserum-Djupedal REE mineralization. **(A) Olserum:** Primary, zoned monazite-(Ce) associated with Th-U-Y-Ca silicate and xenotime-(Y) inclusions. **(B) Djupedal:** Primary, zoned xenotime-(Y) crystal, with small inclusions of monazite-(Ce), uraninite, and thorite concentrated in particular zones of the xenotime-(Y) crystal. **(C) Olserum:** Paragenetically later primary monazite-(Ce) and xenotime-(Y) intergrown with

magnetite. **(D) Olserum:** Large primary fluorapatite crystal with abundant monazite-(Ce) and xenotime-(Y) inclusions. Note the lack of small inclusions in the zone at the center of the BSE image. **(E)** Fine-grained matrix surrounding the primary fluorapatite crystal shown in (D). Monazite-(Ce) and subordinate amounts of xenotime-(Y) are intergrown with magnetite. **(F) Djupedal:** Late-type monazite-(Ce) replacing primary xenotime-(Y) along grain boundaries. Monazite-(Ce) also shows incipient alteration by allanite-(Ce). Mineral abbreviations: aln: allanite; and: andalusite; ap: fluorapatite; bt: biotite; ilm: ilmenite; mag: magnetite; mnz: monazite; qz: quartz; thr: thorite; urn: uraninite; xtm: xenotime.

Figure 6. BSE images from ore assemblages from the Olserum-Djupedal REE mineralization. **(A) Djupedal:** Massive allanite-(Ce) within fractures of primary xenotime-(Y). The massive allanite-(Ce) shows incipient alteration by bastnäsite-(Ce), while minor remobilized late-type monazite-(Ce) occurs as part of the fracture-filling. **(B) Djupedal:** Pervasive replacement of primary monazite-(Ce) by fluorapatite and ferriallanite-(Ce). **(C) Djupedal:** Pervasive replacement of primary monazite-(Ce) with adjacent late-type xenotime-(Y). For additional images of this pervasive alteration, please refer to Fig. EA4 in the Electronic Supplementary Material. **(D) Djupedal:** Late-type monazite-(Ce) showing partial alteration into allanite-(Ce) (replacement-type), fluorapatite, and clinozoisite, close to massive allanite-(Ce). Note the presence of quartz-muscovite symplectites and chloritization of magnetite. Mineral abbreviations: aln: allanite; ap: fluorapatite; bst: bastnäsite; bt: biotite; chl: chlorite; czo: clinozoisite; mag: magnetite; mnz: monazite; ms: muscovite; qz: quartz; xtm: xenotime.

Figure 7. BSE images from ore assemblages from the Olserum-Djupedal REE mineralization. **(A) Djupedal:** Textural manifestation of dissolution-reprecipitation processes in a xenotime-(Y) grain at the boundary of a fluorapatite crystal. BSE-bright zones are enriched in Th, U, and LREE, and depleted in Y, whereas BSE-darker as well as completely dark zones are depleted in

Th, U, LREE, and enriched in Y. Note that the BSE-dark zones host inclusions of Th-U-Y-Pb silicate phases. **(B) Olserum:** Metamict and altered primary (Fe,U,Y,REE,Ca,Si)-(Nb,Ta) oxide with rims of columbite-(Fe) (based on EDS analysis) and xenotime-(Y). **(C) Djupedal:** Alteration of allanite-(Ce) into bastnäsite-(Ce) and chlorite in fracture fillings of primary xenotime-(Y). **(D) Olserum:** Replacement of BMS-hosted allanite-(Ce) into a bastnäsite-(Ce), synchysite-(Ce), and chlorite assemblage containing a small uraninite grain. Mineral abbreviations: aln: allanite; ap: fluorapatite; bst: bastnäsite; bt: biotite; chl: chlorite; col: columbite; crd: cordierite; gn: galena; Kfs: K-feldspar; mag: magnetite; mnz: monazite; ms: muscovite; qz: quartz; syn: synchysite; urn: uraninite; xtm: xenotime.

Figure 8. Diagrams illustrating the major element chemistry of monazite-(Ce). **(A)** Ternary diagram showing monazite-(Ce) composition in LREE-(HREE+Y)-(Th+U) space. **(B)** Variation diagram of Th+U+Si+Pb versus REE+Y+P, illustrating the cheralite ($Ca(Th,U,Pb)REE_{-2}$) and huttonite ($(Th,U,Pb)SiREE_{-1}P_{-1}$) substitution mechanisms in monazite-(Ce).

Figure 9. Normalized (relative to upper continental crust; Rudnick and Gao 2003) REE distribution diagrams for monazite-(Ce) from **(A)** the Olserum mineralization and **(B)** the Djupedal mineralization. Monazite-(Ce) from both schlieren types are shown separately.

Figure 10. Variation diagram of the LREE to HREE slope, $(La/Yb)_N$, as function of the magnitude of the Eu anomaly, Eu/Eu*, for monazite-(Ce), allanite-(Ce), and ferriallanite-(Ce). Pervasively altered monazite-(Ce) shows increased $(La/Yb)_N$ and Eu/Eu* values, whereas partially altered monazite-(Ce) show average $(La/Yb)_N$ values, but higher Eu/Eu* than primary monazite-(Ce). Allanite related to the pervasive alteration shows similar Eu/Eu* as monazite-(Ce). The high $(La/Yb)_N$ values of some primary monazite-(Ce) grains from the Olserum mineralization are probably related to precipitation of small late-type xenotime-(Y).

Figure 11. Diagrams illustrating the major and trace element chemistry of xenotime-(Y). **(A)** Ternary diagram showing xenotime-(Y) composition in Y-HREE-LREE space. **(B)** Variation diagram of (Th+U+Si+Pb) versus (REE+Y+P) highlighting the cheralite and thorite substitution mechanisms in xenotime-(Y). **(C)** Variation diagram of Zr versus Hf showing a good correlation between both elements.

Figure 12. Normalized (relative to upper continental crust; Rudnick and Gao 2003) REE distribution diagrams for xenotime-(Y) from **(A)** the Olserum mineralization and **(B)** the Djupedal mineralization. Xenotime-(Y) related to the breakdown of Nb-Ta oxides and xenotime-(Y) from the biotite-magnetite schlieren are showed separately.

Figure 13. Diagram illustrating the major element composition of allanites and clinozoisite in terms of ∑REE versus Al. The major substitution mechanisms in allanites (Petrík et al. 1995) are shown for reference.

Figure 14. Normalized (relative to upper continental crust; Rudnick and Gao 2003) REE distribution diagram **(A)** for allanite-(Ce), clinozoisite, bastnäsite-(Ce), and synchysite-(Ce) (REE concentration data from EPMA), and corresponding box plots illustrating the magnitude of **(B)** the LREE to HREE slope, $(La/Yb)_N$, **(C)** the Eu anomaly, Eu/Eu*, **(D)** the MREE enrichment, $(La/Sm)_N$, and **(E)** the Y anomaly, Y/Y*.

Figure 15. Variation diagram of F/(F+OH+Cl) versus Ca/(Ca+REE+Y), showing the composition of the analyzed REE-fluorocarbonates.

Tables

Table 1. Calculated temperatures using monazite-xenotime geothermometry.

Type	**Range (°C)**	**Average (°C)**	**SD**	**N**
Primary in Olserum	490-650	580	50	9
Primary in Djupedal	500-570	540	30	5
Granite-hosted veins	550-680	640	40	5
Fluorapatite-associated, inclusions	490-690	630	50	15
Fluorapatite-associated, others	430-700	560	90	26
Late-type	520-670	630	50	8
Biotite-magnetite schlieren	650-660	650	10	2
Quartz-magnetite schlieren	460-590	550	30	13

Figure 1

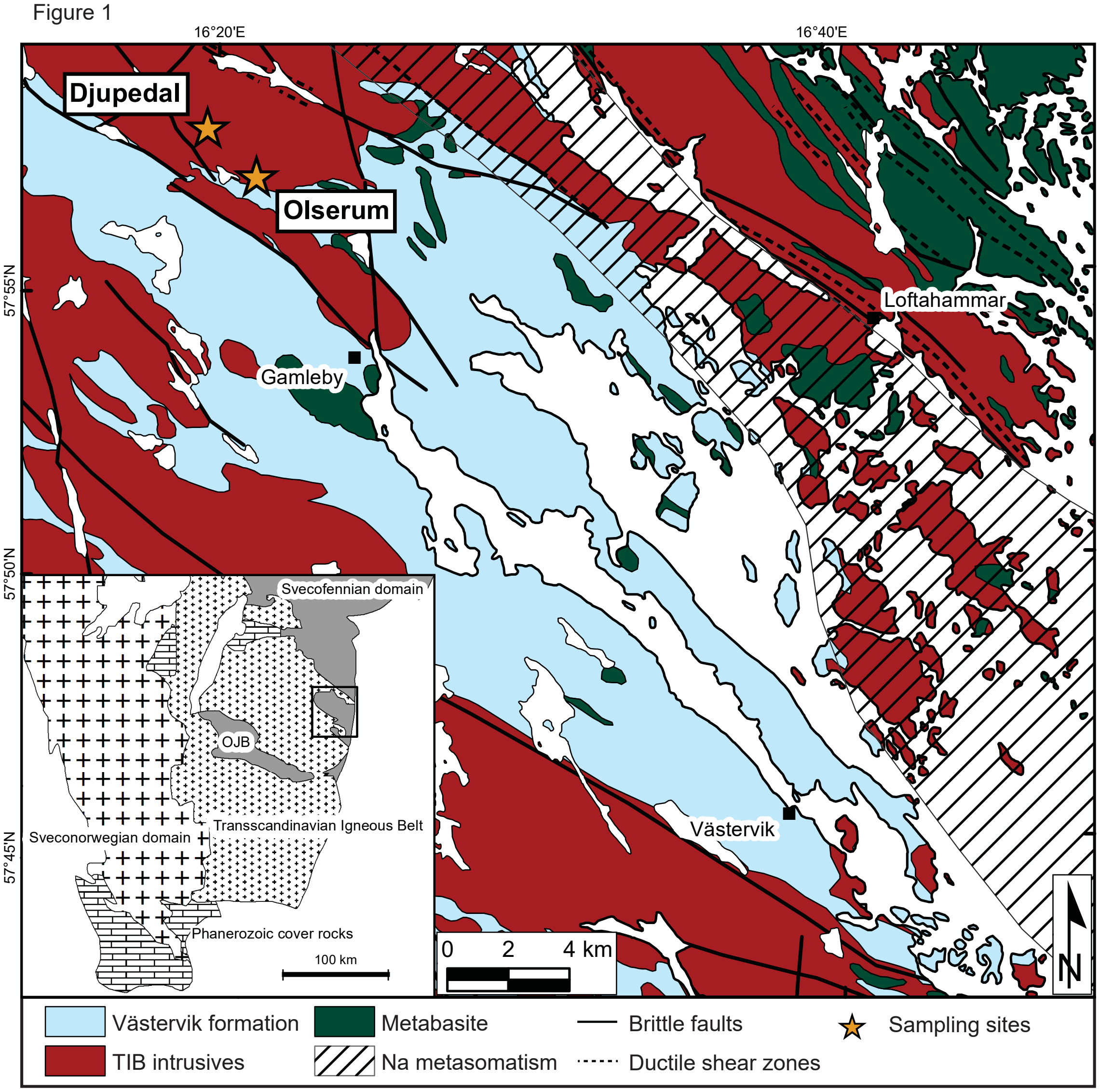
16°20'E
16°40'E
57°55'N
57°50'N
57°45'N
Djupedal
Olserum
Gamleby
Loftahammar
Västervik
Svecofennian domain
OJB
Transscandinavian Igneous Belt
Sveconorwegian domain
Phanerozoic cover rocks
100 km
0 2 4 km
N
Västervik formation
TIB intrusives
Metabasite
Na metasomatism
Brittle faults
Ductile shear zones
Sampling sites

Figure 2

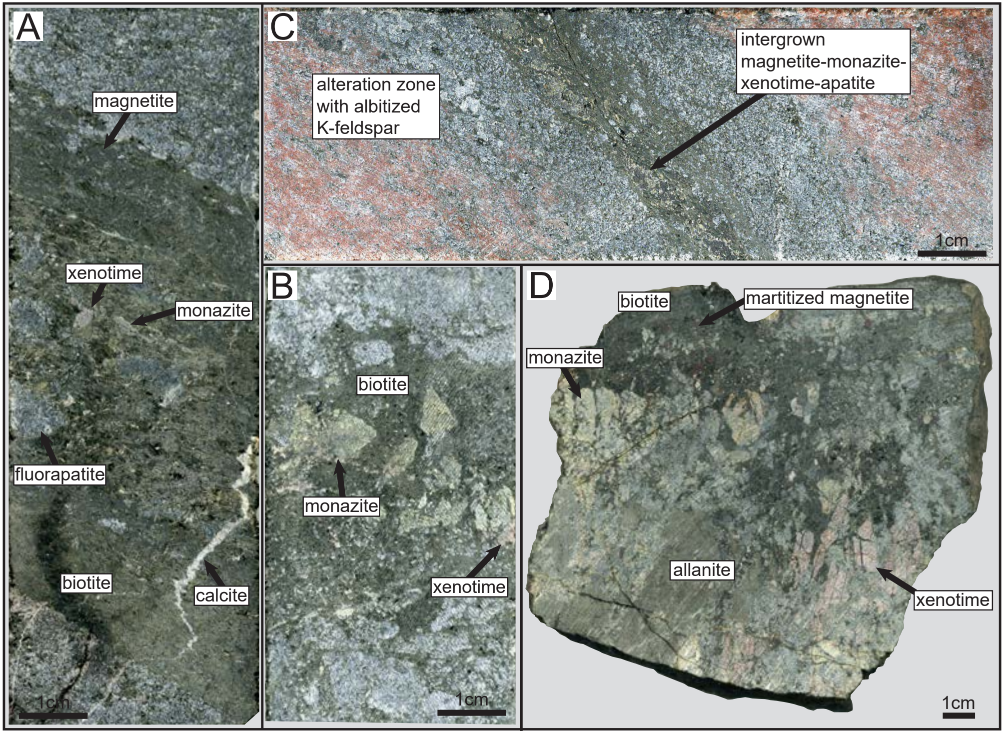
A
magnetite
xenotime
monazite
fluorapatite
biotite
calcite
1cm
C
alteration zone with albitized K-feldspar
intergrown magnetite-monazite-xenotime-apatite
1cm
B
biotite
monazite
xenotime
1cm
D
biotite
martitized magnetite
monazite
allanite
xenotime
1cm

Figure 3

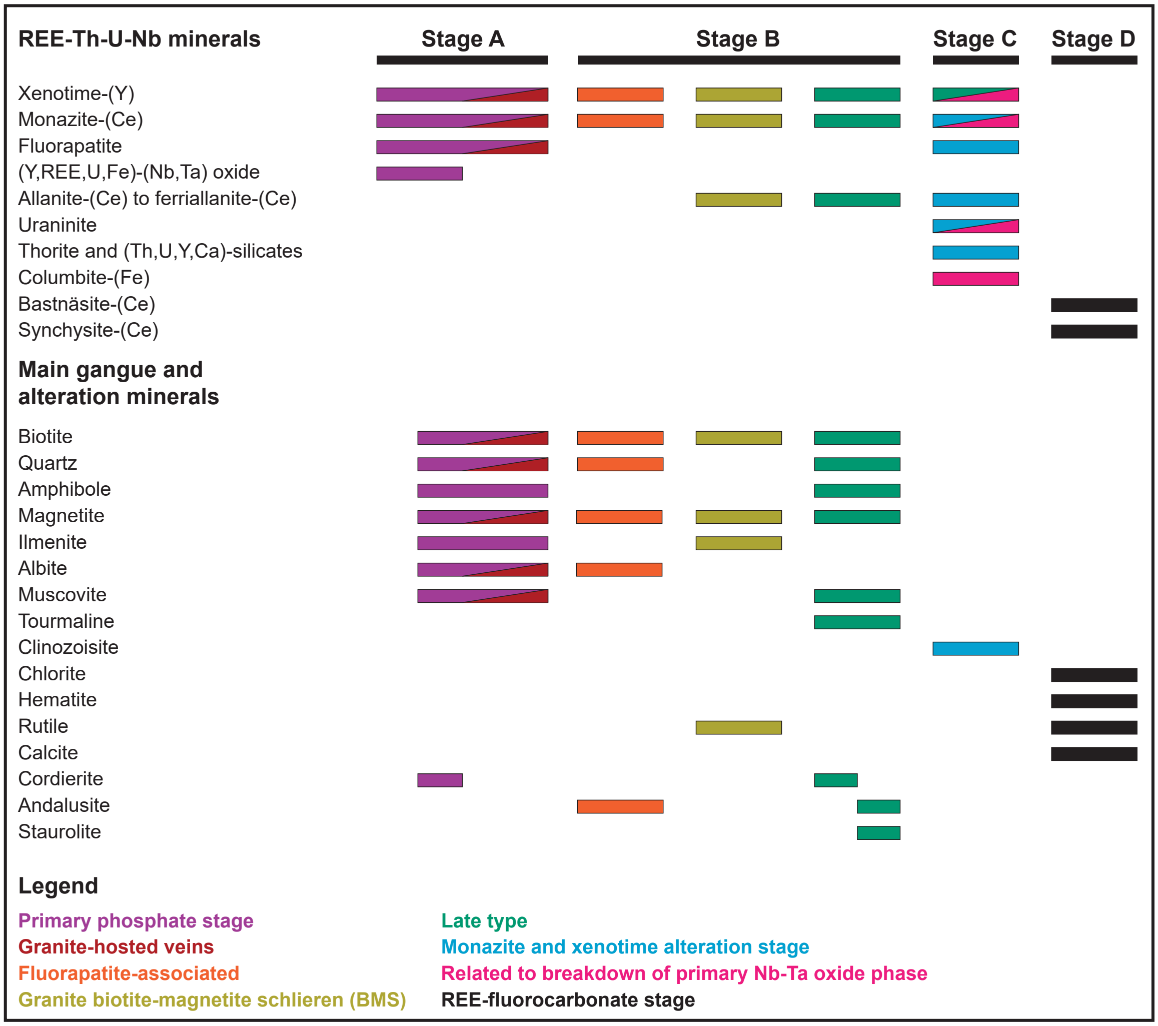
REE-Th-U-Nb minerals
Stage A
Stage B
Stage C
Stage D
Xenotime-(Y)
Monazite-(Ce)
Fluorapatite
(Y,REE,U,Fe)-(Nb,Ta) oxide
Allanite-(Ce) to ferriallanite-(Ce)
Uraninite
Thorite and (Th,U,Y,Ca)-silicates
Columbite-(Fe)
Bastnäsite-(Ce)
Synchysite-(Ce)
Main gangue and alteration minerals
Biotite
Quartz
Amphibole
Magnetite
Ilmenite
Albite
Muscovite
Tourmaline
Clinozoisite
Chlorite
Hematite
Rutile
Calcite
Cordierite
Andalusite
Staurolite
Legend
Primary phosphate stage
Granite-hosted veins
Fluorapatite-associated
Granite biotite-magnetite schlieren (BMS)
Late type
Monazite and xenotime alteration stage
Related to breakdown of primary Nb-Ta oxide phase
REE-fluorocarbonate stage

Figure 4

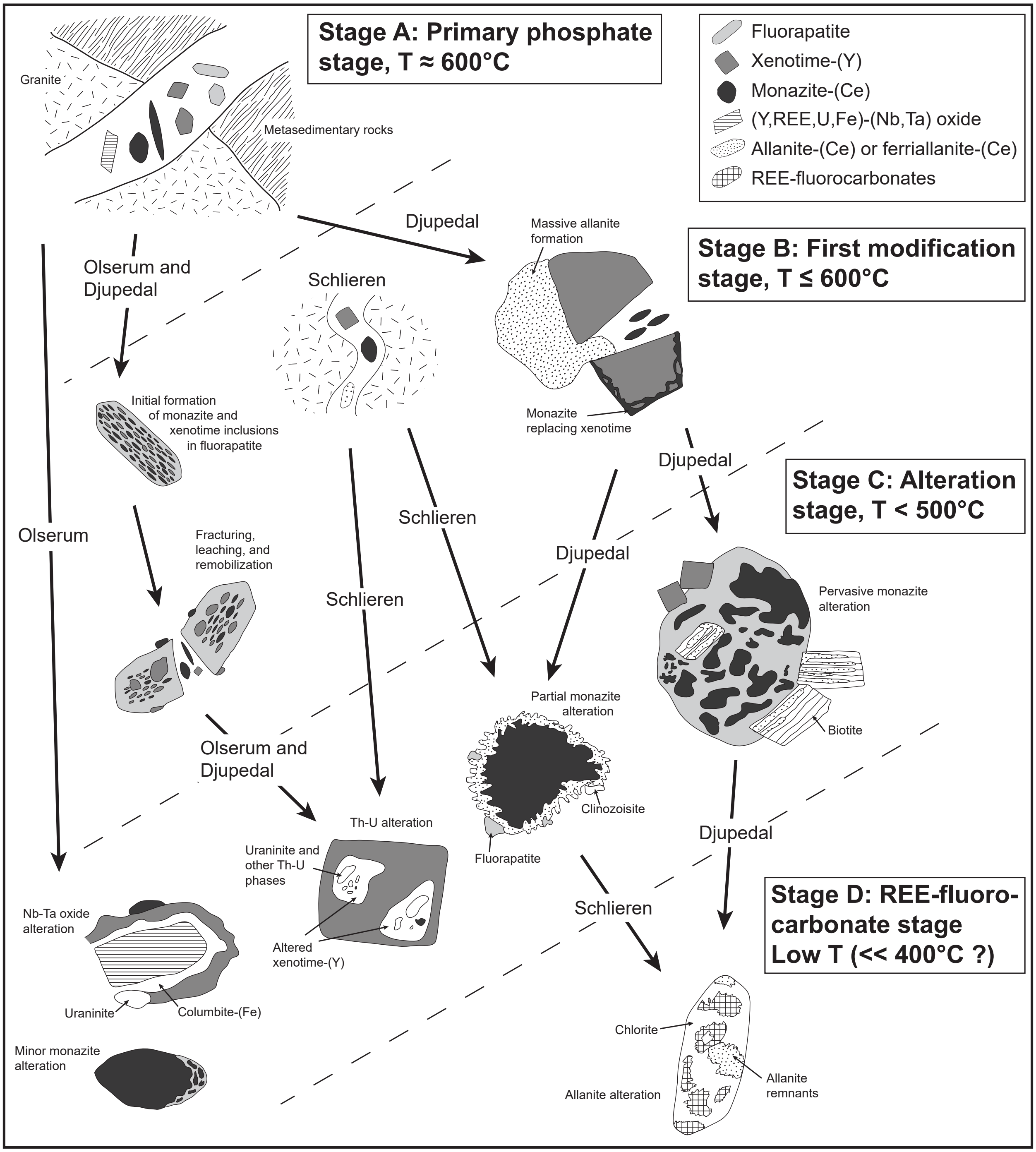
Stage A: Primary phosphate stage, T ≈ 600°C
Fluorapatite
Xenotime-(Y)
Monazite-(Ce)
(Y,REE,U,Fe)-(Nb,Ta) oxide
Allanite-(Ce) or ferriallanite-(Ce)
REE-fluorocarbonates
Granite
Metasedimentary rocks
Djupedal
Massive allanite formation
Stage B: First modification stage, T ≤ 600°C
Olserum and Djupedal
Schlieren
Initial formation of monazite and xenotime inclusions in fluorapatite
Monazite replacing xenotime
Djupedal
Stage C: Alteration stage, T < 500°C
Olserum
Schlieren
Fracturing, leaching, and remobilization
Djupedal
Schlieren
Pervasive monazite alteration
Biotite
Partial monazite alteration
Clinozoisite
Fluorapatite
Olserum and Djupedal
Th-U alteration
Uraninite and other Th-U phases
Altered xenotime-(Y)
Djupedal
Schlieren
Stage D: REE-fluoro-carbonate stage Low T (<< 400°C ?)
Nb-Ta oxide alteration
Uraninite
Columbite-(Fe)
Minor monazite alteration
Chlorite
Allanite remnants
Allanite alteration

Figure 5

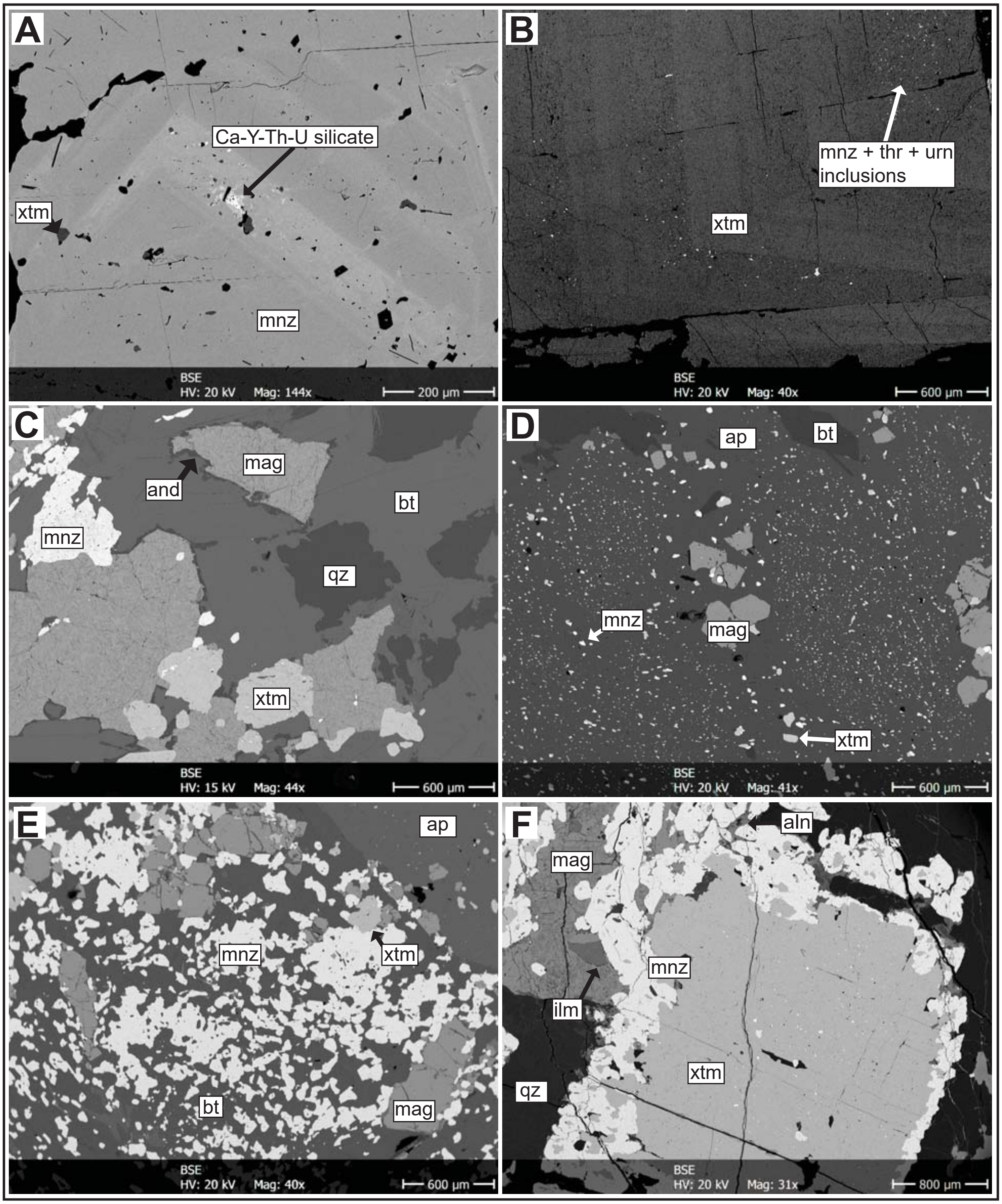
A
Ca-Y-Th-U silicate
xtm
mnz
BSE
HV: 20 kV Mag: 144x
200 µm
B
mnz + thr + urn inclusions
xtm
BSE
HV: 20 kV Mag: 40x
600 µm
C
mag
and
bt
mnz
qz
xtm
BSE
HV: 15 kV Mag: 44x
600 µm
D
ap
bt
mnz
mag
xtm
BSE
HV: 20 kV Mag: 41x
600 µm
E
ap
mnz
xtm
bt
mag
BSE
HV: 20 kV Mag: 40x
600 µm
F
aln
mag
mnz
ilm
xtm
qz
BSE
HV: 20 kV Mag: 31x
800 µm

Figure 6

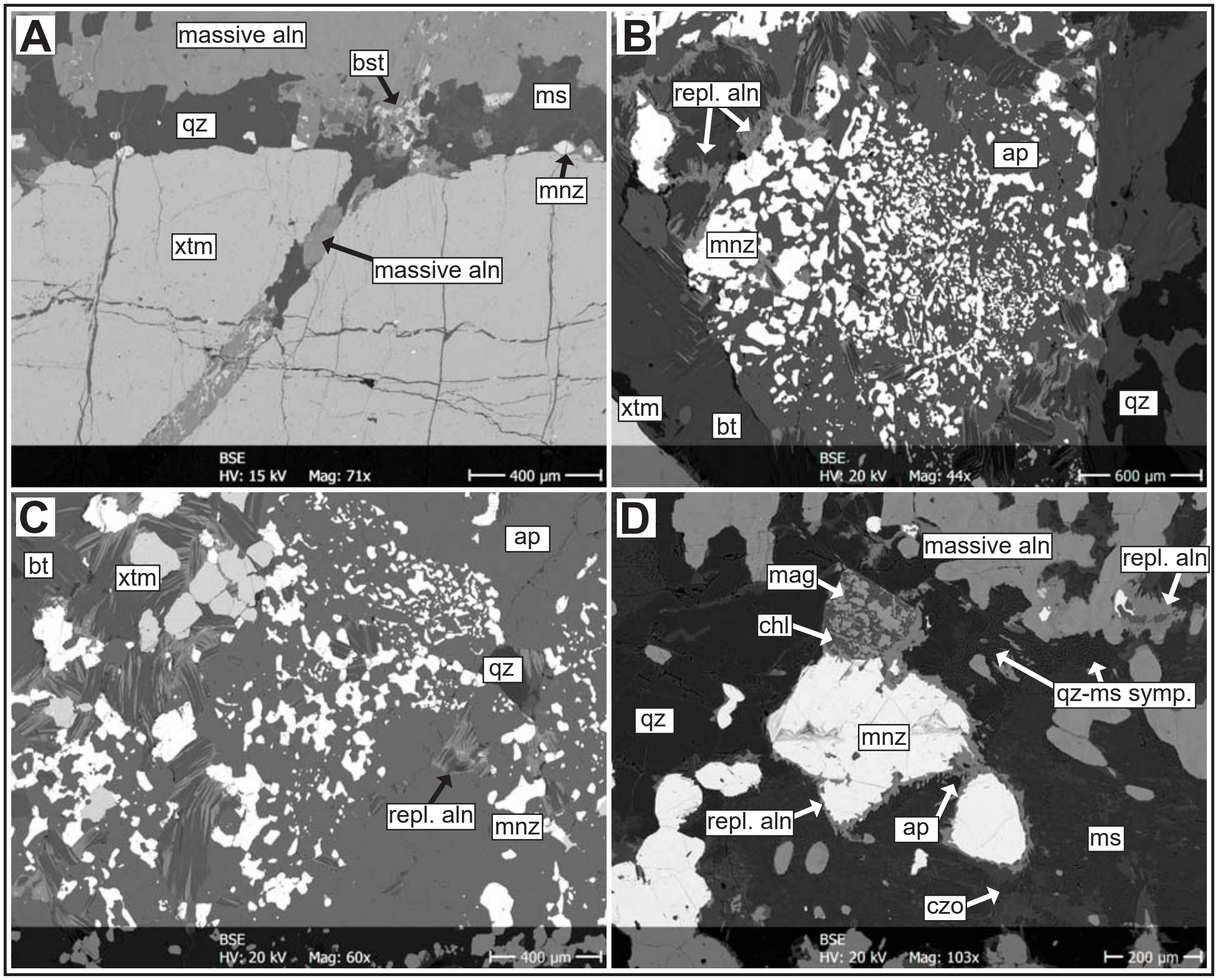
A
massive aln
bst
ms
qz
mnz
xtm
massive aln
BSE
HV: 15 kV Mag: 71x
400 µm
B
repl. aln
ap
mnz
xtm
bt
qz
BSE
HV: 20 kV Mag: 44x
600 µm
C
ap
bt
xtm
qz
repl. aln
mnz
BSE
HV: 20 kV Mag: 60x
400 µm
D
massive aln
repl. aln
mag
chl
qz-ms symp.
qz
mnz
repl. aln
ap
ms
czo
BSE
HV: 20 kV Mag: 103x
200 µm

Figure 7

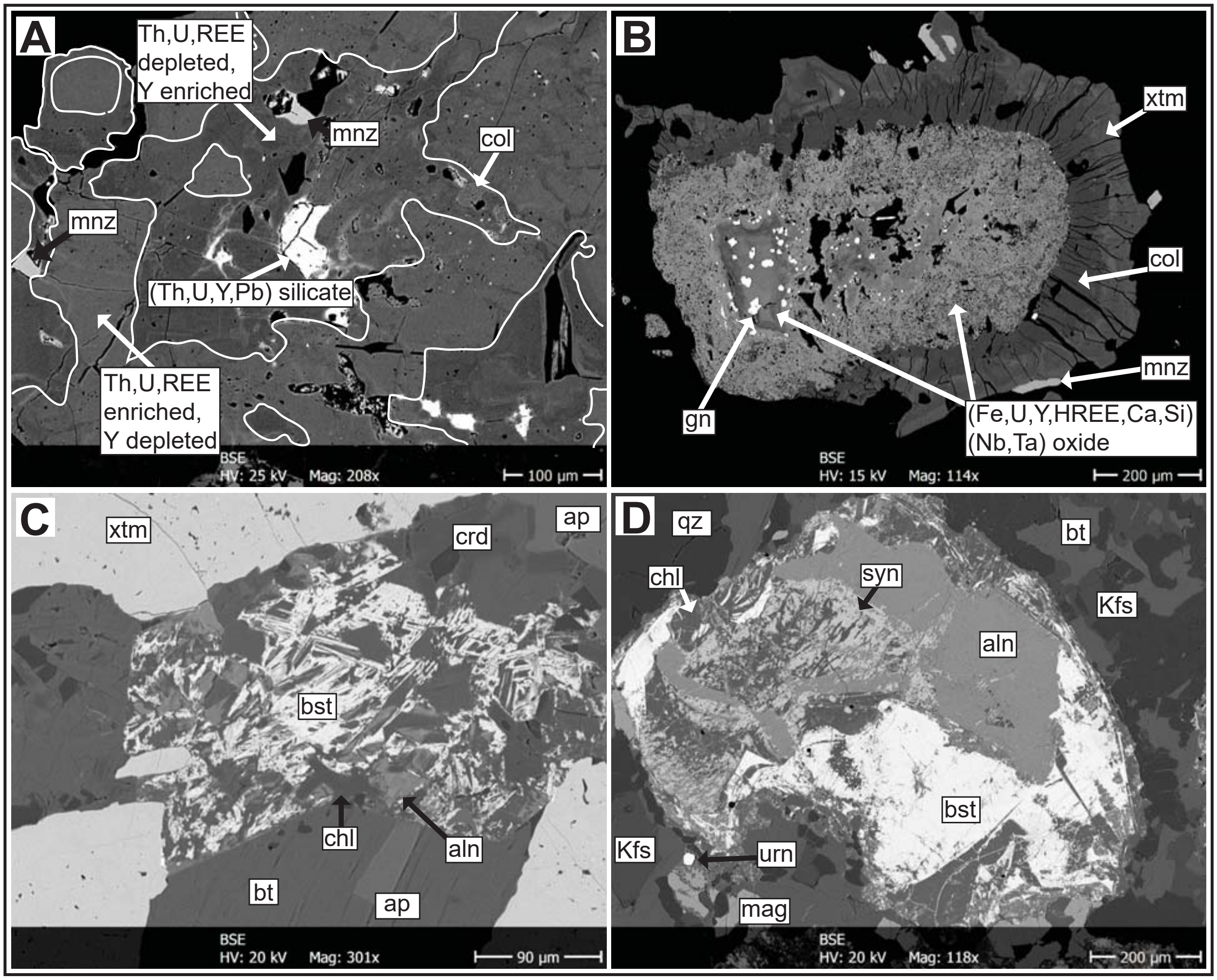
A
Th,U,REE depleted, Y enriched
mnz
col
mnz
(Th,U,Y,Pb) silicate
Th,U,REE enriched, Y depleted
BSE
HV: 25 kV Mag: 208x
100 µm
B
xtm
col
mnz
gn
(Fe,U,Y,HREE,Ca,Si) (Nb,Ta) oxide
BSE
HV: 15 kV Mag: 114x
200 µm
C
xtm
crd
ap
bst
chl
aln
bt
ap
BSE
HV: 20 kV Mag: 301x
90 µm
D
qz
bt
chl
syn
Kfs
aln
bst
Kfs
urn
mag
BSE
HV: 20 kV Mag: 118x
200 µm

Figure 8

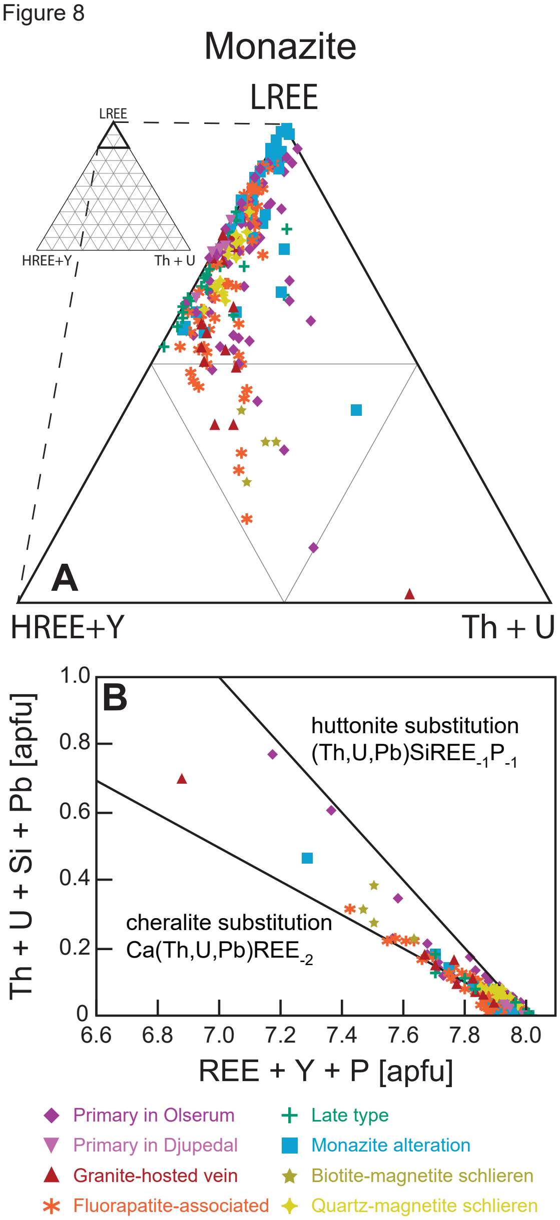
Monazite
LREE
LREE
HREE+Y
Th + U
A
HREE+Y
Th + U
B
huttonite substitution
(Th,U,Pb)SiREE$_{-1}$P$_{-1}$
cheralite substitution
Ca(Th,U,Pb)REE$_{-2}$
Th + U + Si + Pb [apfu]
1.0
0.8
0.6
0.4
0.2
0
6.6
6.8
7.0
7.2
7.4
7.6
7.8
8.0
REE + Y + P [apfu]
◆ Primary in Olserum
▼ Primary in Djupedal
▲ Granite-hosted vein
✱ Fluorapatite-associated
+ Late type
■ Monazite alteration
★ Biotite-magnetite schlieren
✦ Quartz-magnetite schlieren

Figure 9

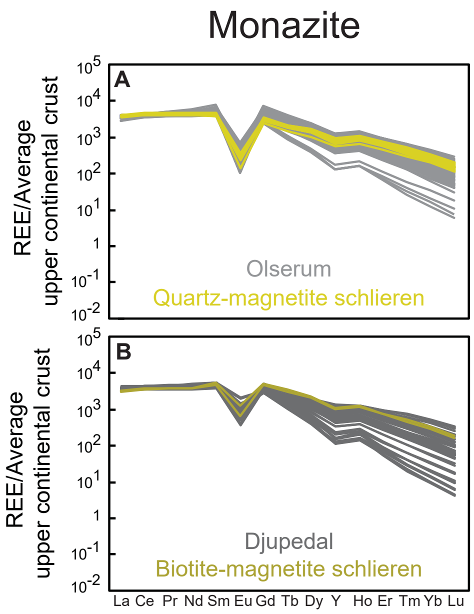
Monazite
A
B
REE/Average upper continental crust
REE/Average upper continental crust
10^5
10^4
10^3
10^2
10^1
1
10^{-1}
10^{-2}
Olserum
Quartz-magnetite schlieren
Djupedal
Biotite-magnetite schlieren
La Ce Pr Nd Sm Eu Gd Tb Dy Y Ho Er Tm Yb Lu

Figure 10

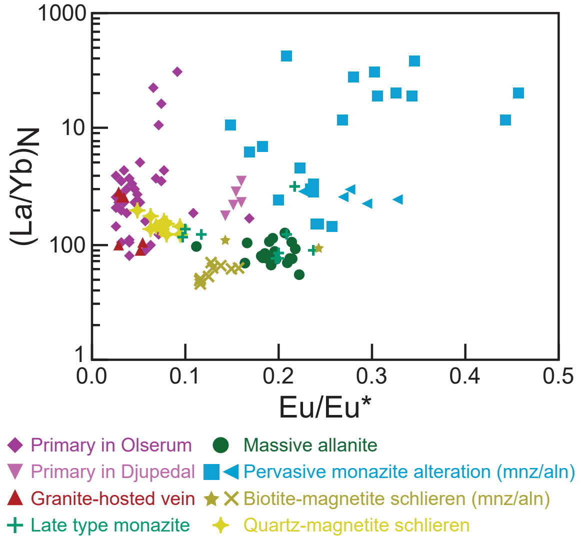
1000
10
100
1
(La/Yb)N
0.0
0.1
0.2
0.3
0.4
0.5
Eu/Eu*
Primary in Olserum
Massive allanite
Primary in Djupedal
Pervasive monazite alteration (mnz/aln)
Granite-hosted vein
Biotite-magnetite schlieren (mnz/aln)
Late type monazite
Quartz-magnetite schlieren

Figure 11

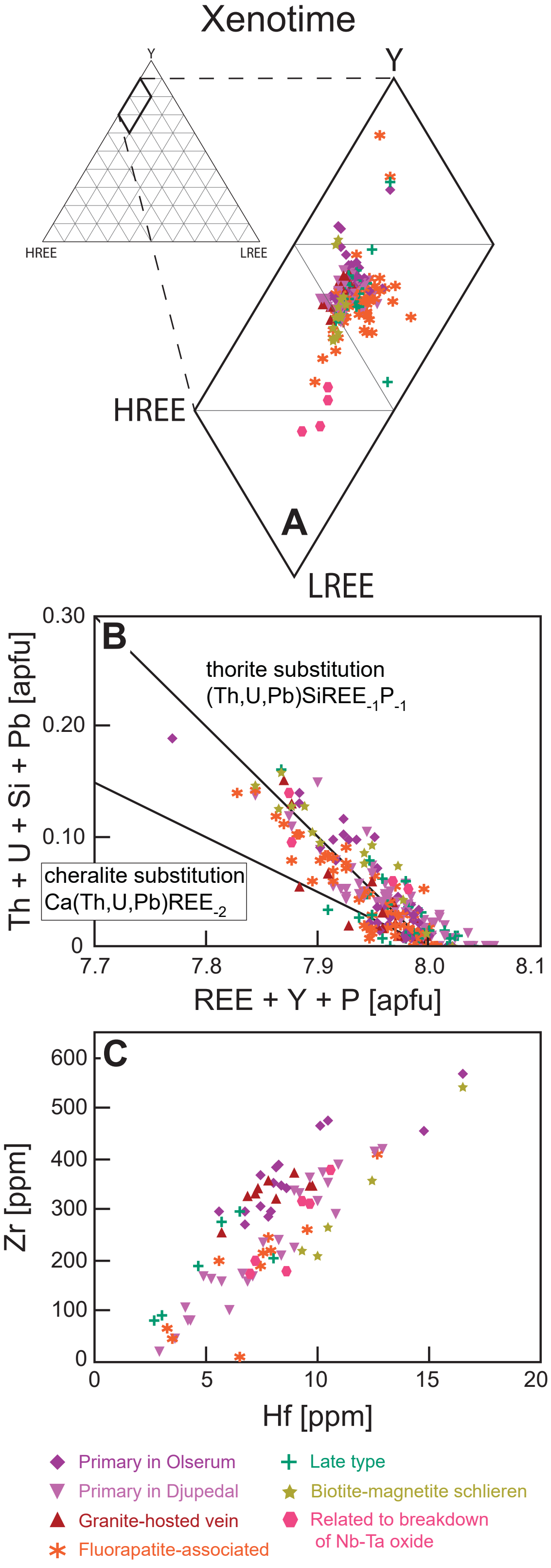
Xenotime
Y
HREE
LREE
Y
HREE
A
LREE
B
thorite substitution
(Th,U,Pb)SiREE$_{-1}$P$_{-1}$
cheralite substitution
Ca(Th,U,Pb)REE$_{-2}$
0.30
0.20
0.10
0
7.7
7.8
7.9
8.0
8.1
Th + U + Si + Pb [apfu]
REE + Y + P [apfu]
C
600
500
400
300
200
100
0
0
5
10
15
20
Zr [ppm]
Hf [ppm]
Primary in Olserum
Primary in Djupedal
Granite-hosted vein
Fluorapatite-associated
Late type
Biotite-magnetite schlieren
Related to breakdown of Nb-Ta oxide

Figure 12

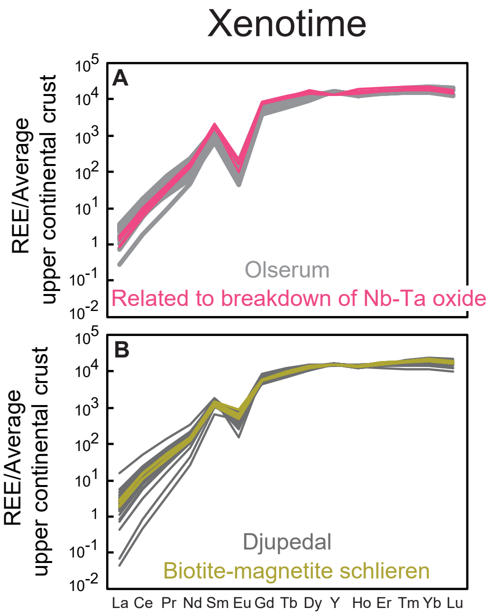
Xenotime
A
REE/Average upper continental crust
10^5
10^4
10^3
10^2
10^1
1
10^{-1}
10^{-2}
Olserum
Related to breakdown of Nb-Ta oxide
B
REE/Average upper continental crust
Djupedal
Biotite-magnetite schlieren
La Ce Pr Nd Sm Eu Gd Tb Dy Y Ho Er Tm Yb Lu

Figure 13

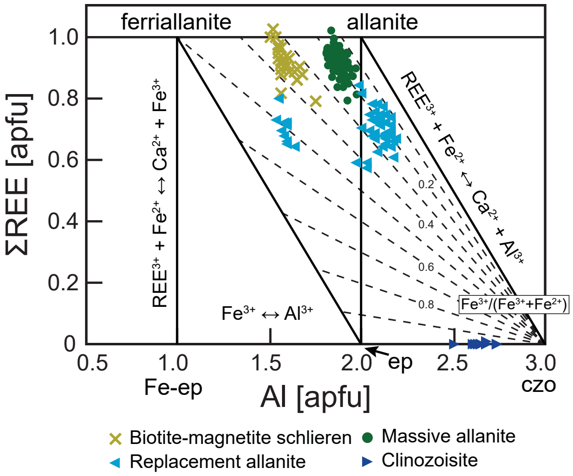
ferriallanite
allanite
1.0
0.8
0.6
0.4
0.2
0
ΣREE [apfu]
REE³⁺ + Fe²⁺ ↔ Ca²⁺ + Fe³⁺
REE³⁺ + Fe²⁺ ↔ Ca²⁺ + Al³⁺
Fe³⁺ ↔ Al³⁺
0.2
0.4
0.6
0.8
Fe³⁺/(Fe³⁺+Fe²⁺)
0.5
1.0
Fe-ep
1.5
2.0
ep
2.5
3.0
czo
Al [apfu]
× Biotite-magnetite schlieren
● Massive allanite
◀ Replacement allanite
▶ Clinozoisite

Figure 14

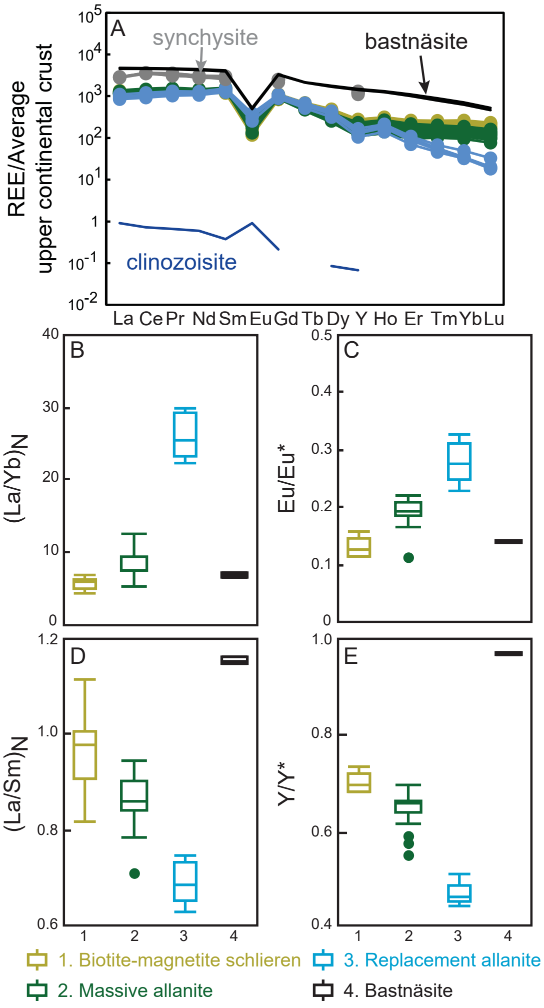
A
synchysite
bastnäsite
clinozoisite
REE/Average upper continental crust
10^5
10^4
10^3
10^2
10^1
1
10^{-1}
10^{-2}
La Ce Pr Nd Sm Eu Gd Tb Dy Y Ho Er Tm Yb Lu
B
$(La/Yb)_N$
0
10
20
30
40
C
Eu/Eu*
0
0.1
0.2
0.3
0.4
0.5
D
$(La/Sm)_N$
0.6
0.8
1.0
1.2
E
Y/Y*
0.4
0.6
0.8
1.0
1
2
3
4
1. Biotite-magnetite schlieren
2. Massive allanite
3. Replacement allanite
4. Bastnäsite

Figure 15

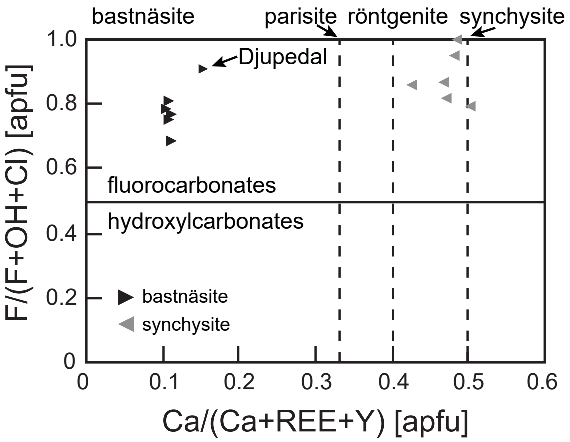
bastnäsite
parisite
röntgenite
synchysite
Djupedal
fluorocarbonates
hydroxylcarbonates
▶ bastnäsite
◀ synchysite
F/(F+OH+Cl) [apfu]
0
0.2
0.4
0.6
0.8
1.0
Ca/(Ca+REE+Y) [apfu]
0
0.1
0.2
0.3
0.4
0.5
0.6